



# An epilepsy-associated $K_v1.2$ charge-transfer-center mutation impairs $K_v1.2$ and $K_v1.4$ trafficking

Michelle Nilsson<sup>a</sup>, Sarah H. Lindström<sup>a</sup>, Maki Kaneko<sup>b,c</sup>, Kaiqian Wang<sup>a</sup>, Teresa Minguez-Viñas<sup>a</sup>, Marina Angelini<sup>d</sup>, Federica Steccanella<sup>d</sup>, Deborah Holder<sup>e</sup>, Michela Ottolia<sup>d,f</sup>, Riccardo Olcese<sup>d,f,g,h</sup>, and Antonios Pantazis<sup>a,i,1</sup>

Edited by Lily Jan, HHMI, University of California, San Francisco, CA; received July 26, 2021; accepted February 25, 2022

We report on a heterozygous *KCNA2* variant in a child with epilepsy. *KCNA2* encodes  $K_v1.2$  subunits, which form homotetrameric potassium channels and participate in heterotetrameric channel complexes with other  $K_v1$ -family subunits, regulating neuronal excitability. The mutation causes substitution F233S at the  $K_v1.2$  charge transfer center of the voltage-sensing domain. Immunocytochemical trafficking assays showed that  $K_v1.2$ (F233S) subunits are trafficking deficient and reduce the surface expression of wild-type  $K_v1.2$  and  $K_v1.4$ : a dominant-negative phenotype extending beyond *KCNA2*, likely profoundly perturbing electrical signaling. Yet some  $K_v1.2$ (F233S) trafficking was rescued by wild-type  $K_v1.2$  and  $K_v1.4$  subunits, likely in permissible heterotetrameric stoichiometries: electrophysiological studies utilizing applied transgenomics and concatamer constructs support that up to one or two  $K_v1.2$ (F233S) subunits can participate in trafficking-capable heterotetramers with wild-type  $K_v1.2$  or  $K_v1.4$ , respectively, and that both early and late events along the biosynthesis and secretion pathway impair trafficking. These studies suggested that F233S causes a depolarizing shift of  $\sim 48$  mV on  $K_v1.2$  voltage dependence. Optical tracking of the  $K_v1.2$ (F233S) voltage-sensing domain (rescued by wild-type  $K_v1.2$  or  $K_v1.4$ ) revealed that it operates with modestly perturbed voltage dependence and retains pore coupling, evidenced by off-charge immobilization. The equivalent mutation in the Shaker  $K^+$  channel (F290S) was reported to modestly affect trafficking and strongly affect function: an  $\sim 80$ -mV depolarizing shift disrupted voltage sensor activation and pore coupling. Our work exposes the multigenic, molecular etiology of a variant associated with epilepsy and reveals that charge-transfer-center disruption has different effects in  $K_v1.2$  and Shaker, the archetypes for potassium channel structure and function.

ion channel | channelopathy | fluorometry | trafficking | dominant negative

A child patient with epileptic seizures has a de novo, missense, heterozygous mutation c.698T > C in *KCNA2*. *KCNA2* encodes  $K_v1.2$  voltage-gated potassium channel subunits (1), which are expressed in central neurons and primarily localized to axon initial segments, juxtaparanodes, and axon preterminals (2).  $K_v1.2$  channels form a delayed rectifier conductance that regulates action potential repolarization, contributing to firing frequency and synaptic transmission (2–4). Neuronal firing behavior can be further modulated by  $K_v1.2$ -subunit interaction with other  $K_v1$  subunits: e.g., an A-type conductance is formed by  $K_v1.2$  and  $K_v1.4$  heteromeric channels (3, 5, 6). A growing number of both gain- and loss-of-function *KCNA2* variants are implicated in epileptic encephalopathy (7–10).

The mutation causes substitution F233S at the second (S2) transmembrane helix of  $K_v1.2$  (Fig. 1A). Located within the voltage-sensing domain (VSD), F233 is part of the charge transfer center critical for voltage sensitivity (Fig. 1B) (11, 13, 20). The equivalent mutation (F290S) in the Shaker  $K_v$  channel from *Drosophila* impairs voltage-dependent channel opening (11) by disrupting the final VSD activation transition, which couples VSD activation to pore opening (13). However, no investigation of the same mutation has been published in the  $K_v1.2$  channel, even though the  $K_v1.2$ -2.1 channel chimera (which encompasses the  $K_v1.2$  F233 site) is the gold standard for potassium channel structure (11, 21). We sought to characterize the effects of mutation F233S in  $K_v1.2$ , as well as its neuronal molecular partner,  $K_v1.4$ .

## Results

**Discovery of a *KCNA2* Variant in a Patient with Epilepsy.** The proband is a male infant with onset, at 15 mo, of a febrile generalized convulsive seizure that lasted 5 min. The second seizure (20 mo), febrile status epilepticus, lasted 45 min. The third seizure (23 mo)

## Significance

A child with epilepsy has a previously unreported, heterozygous mutation in *KCNA2*, the gene encoding  $K_v1.2$  proteins. Four  $K_v1.2$  assemble into a potassium-selective channel, a protein complex at the neuronal cell surface regulating electrical signaling.  $K_v1.2$  subunits assemble with other  $K_v1$ -family members to form heterotetrameric channels, contributing to neuronal potassium-channel diversity. The most striking consequence of this mutation is preventing  $K_v1.2$ -subunit trafficking, i.e., their ability to reach the cell surface. Moreover, the mutation is dominant negative, as mutant subunits can assemble with wild-type  $K_v1.2$  and  $K_v1.4$ , trapping them into nontrafficking heterotetramers and decreasing their functional expression. Thus,  $K_v1$ -family genes' ability to form heterotetrameric channels is a double-edged sword, rendering  $K_v1$ -family members vulnerable to dominant-negative mutations in a single member gene.

Author contributions: M.O., R.O., and A.P. designed research; M.N., S.H.L., M.K., K.W., T.M.-V., M.A., F.S., D.H., and A.P. performed research; M.N., S.H.L., K.W., T.M.-V., M.O., and A.P. contributed new reagents/analytic tools; M.N., S.H.L., M.K., K.W., T.M.-V., D.H., and A.P. analyzed data; and M.N., S.H.L., M.K., D.H., M.O., R.O., and A.P. wrote the paper.

The authors declare no competing interest.

This article is a PNAS Direct Submission.

Copyright © 2022 the Author(s). Published by PNAS. This open access article is distributed under Creative Commons Attribution License 4.0 (CC BY).

<sup>1</sup>To whom correspondence may be addressed. Email: antonios.pantazis@liu.se.

This article contains supporting information online at <http://www.pnas.org/lookup/suppl/doi:10.1073/pnas.2113675119/-DCSupplemental>.

Published April 19, 2022.

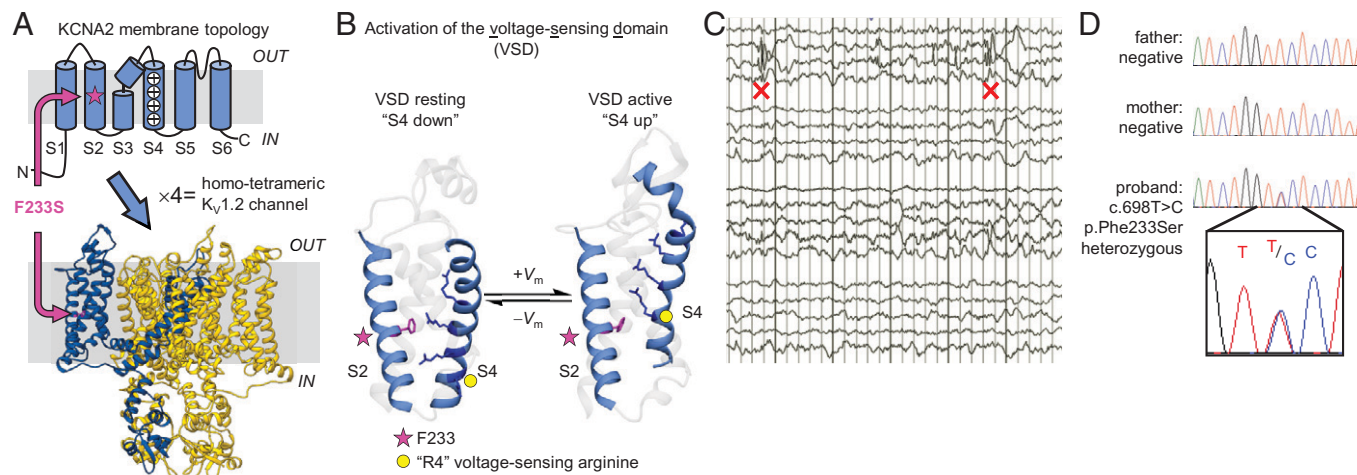


**Fig. 1.** Discovery of a *KCNA2* mutation in a patient with epilepsy. (A) Membrane topology of the Kv1.2 subunit and model of a homotetrameric Kv1.2 channel (8). F233S is on helix S2, within the VSD. (B) Model of Kv1.2 VSD activation and deactivation (8). The electric field is focused on F233 (magenta, star symbol), which is part of the charge transfer center (11). Upon membrane depolarization (+V<sub>m</sub>), positively charged residues on S4 [side chains in dark blue (12)], traverse the membrane electric field, compelling S4 to move outward. Movement of the fourth conserved arginine R4 is thought to couple VSD activation to pore opening (13, 14). Upon membrane repolarization (−V<sub>m</sub>), S4 returns to its resting state, inducing pore closure (15–19). (C) Partial EEG of the sleeping patient, showing right posterior epileptiform discharges (red X). (D) Sequencing chromatograms of the patient and his healthy parents. Inset: Magnified view at the mutation site (*KCNA2* c.698T > C, heterozygous).

was prolonged status epilepticus associated with roseola infection and fever, whereupon he was hospitalized with intubation. The initial electroencephalogram (EEG) showed right hemispheric slowing; a follow-up EEG showed right posterior temporal slowing and multifocal spikes (Fig. 1C). The proband continued to have occasional seizures, often associated with illness and fever and usually requiring rescue medication. His development has been delayed with some mild autistic features. The patient was screened with an exome-based DNA panel of 224 epilepsy-associated genes (SI Appendix, Table S1). A heterozygous c.698T > C (p.Phe233Ser) missense change in *KCNA2* (transcript: NM\_004974.3) was identified. The variant was confirmed in the patient by Sanger sequencing. Targeted Sanger sequencing of DNA from parents showed its de novo origin (Fig. 1D). This variant has not been recorded in population databases [the genome aggregation database and the exome aggregation consortium (22), ClinVar (23), and the human gene mutation database (24)] and was classified as potentially deleterious by the Sorting Intolerant from Tolerant (SIFT) (25) and MutationTester2 (26) prediction algorithms. No other pathogenic variants were found.

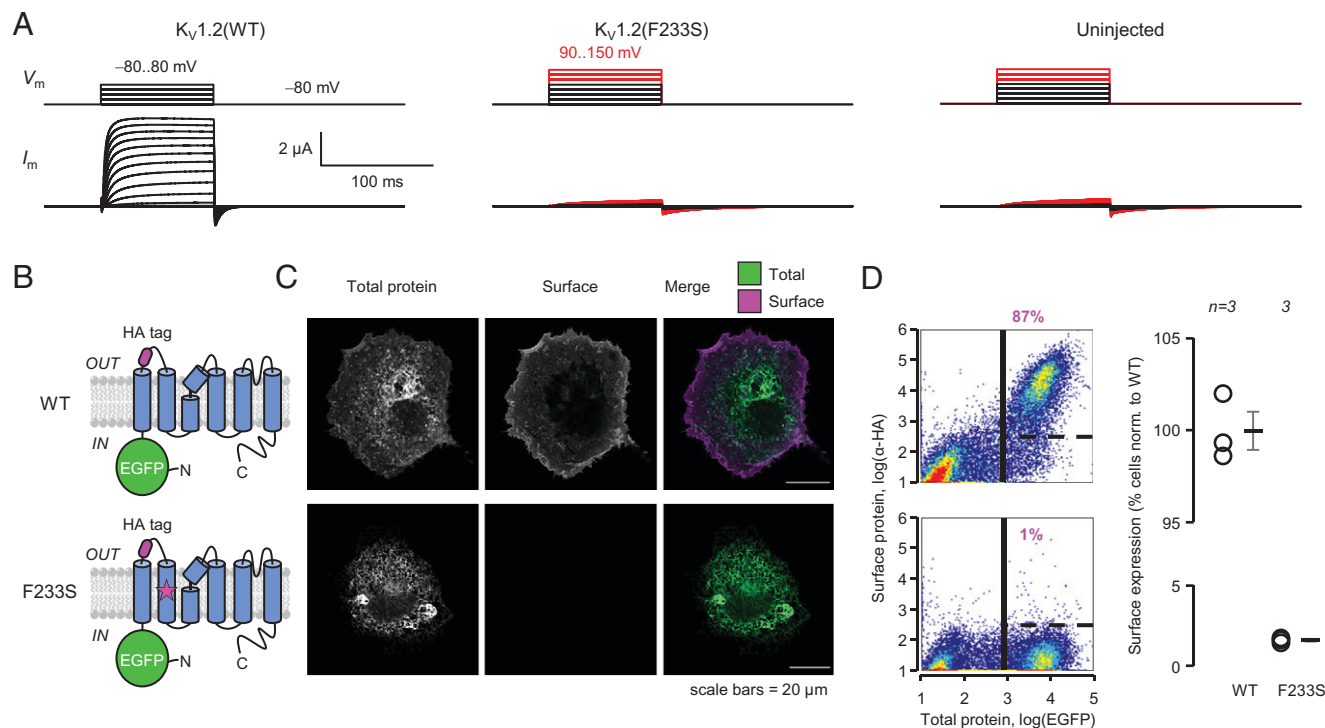
**F233S Completely Prevents the Cell-Surface Trafficking of Kv1.2 Channels.** Electrophysiological experiments in *Xenopus* oocytes injected with Kv1.2(F233S) complementary ribonucleic acid (cRNA) revealed no detectable current (Fig. 2A). To differentiate between a severe functional or trafficking deficiency, we performed trafficking assays in mammalian COS-7 cells, as previously (8). Cells were transfected with wild-type (WT) or F233S Kv1.2 constructs (Fig. 2B) reporting both total and surface protein (27). These experiments showed that Kv1.2(F233S) subunits do not traffic to the cell surface (Fig. 2C and D).

**Kv1.2(F233S) Subunits Cause a Dominant-Negative Suppression of Kv1.2 Channel Conductance.** As the patient is heterozygous, both WT and F233S-bearing Kv1.2 subunits are present in his neurons and could tetramerize during early biogenesis as nascent polypeptides (28). We injected different amounts of WT and F233S cRNA in *Xenopus* oocytes to emulate homozygous WT (double cRNA dose corresponding to two WT alleles), half-

dose WT (single cRNA dose corresponding to one WT allele), heterozygous (single WT and single F233S cRNA doses), and homozygous mutant (double F233S cRNA dose). The cells responded linearly to injected cRNA, exhibiting  $0.57 \pm 0.07$ -fold conductance in the half-dose WT condition compared to homozygous WT ( $1.0 \pm 0.098$ ) (Fig. 3A and B). The former was not significantly different from a theoretical sample with mean 0.5 and the same  $\sigma$  and  $n$  ( $P = 0.50$ ). Heterozygous cells exhibited ~20% conductance compared to homozygous-WT cells, significantly less than half-dose WT ( $P = 1.3 \times 10^{-5}$ ), demonstrating dominant-negative loss of Kv1.2 function. The current in these conditions had similar voltage dependence (Fig. 3C), indicating that the main effect of F233S is its trafficking defect. Homozygous-mutant cells produced no current (Fig. 3A and D).

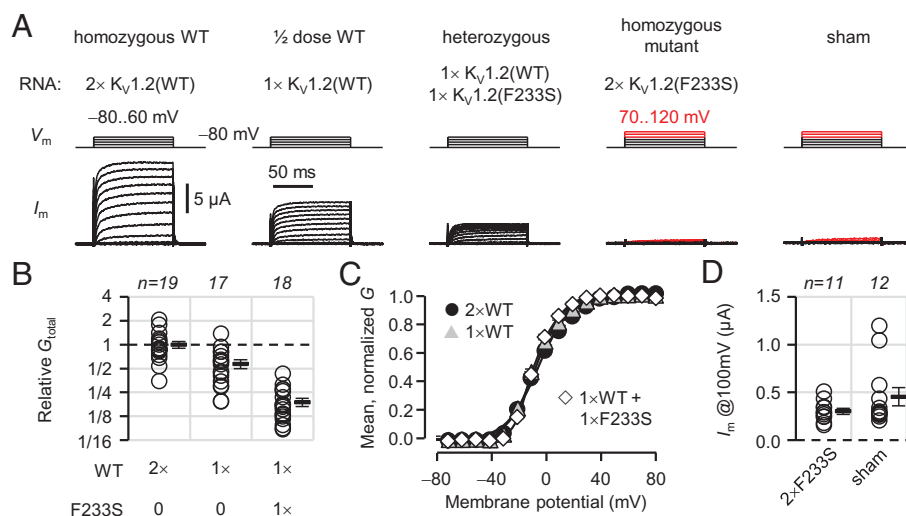
**Kv1.2(F233S) Subunits Sequester, and Are Concomitantly Rescued by, Kv1.2(WT).** The dominant-negative loss of Kv1.2 conductance is likely due to the association of WT and trafficking-deficient F233S subunits, decreasing the availability of the former on the cell surface. We directly evaluated surface trafficking of WT subunits in the presence of either WT or F233S subunits, and vice versa, by flow cytometry. COS-7 cells were transfected with two Kv1.2 constructs in equal proportion, representing two *KCNA2* alleles, each bearing a different pair of tags reporting total and surface protein expression (Fig. 4A). We evaluated surface expression in live cells positive for both total protein tags (Fig. 4B). When a Kv1.2(WT) was coexpressed with another Kv1.2(WT) construct, it exhibited high surface expression. Crucially, Kv1.2(WT) trafficking was significantly reduced in the presence of Kv1.2(F233S).

The previous result suggests that WT and F233S subunits can assemble into trafficking-deficient heterotetramers. Is it possible that a different fraction of WT/F233S heterotetramers can reach the surface? Indeed, a significant amount of F233S subunits were detected on the surface of cells coexpressing WT, indicating rescue (Fig. 4B). The same results were obtained using the oppositely labeled constructs, although bungarotoxin signals were weaker than those from hemagglutinin-tagged constructs (SI Appendix, Fig. S1).



**Only  $K_v1.2$ (WT/F233S) Heterotetramers with One F233S Subunit Are Likely Trafficking Competent.** The results so far suggest that some  $K_v1.2$ (WT/F233S) heterotetramers are trafficking deficient, causing WT-subunit sequestration, while others are trafficking competent, causing F233S-subunit rescue. Since the N-terminal tetramerization domain of  $K_v1$  subunits facilitates oligomerization early in

biosynthesis (28), one would expect the full complement of tetrameric WT/F233S stoichiometries to form. Could it be that only specific stoichiometries are trafficking competent? To direct the distribution of tetrameric stoichiometries, we implemented an “applied transcriptomics” experimental paradigm, varying the molar proportion of  $K_v1.2$ (F233S) RNA injected in oocytes over a broad range while keeping the





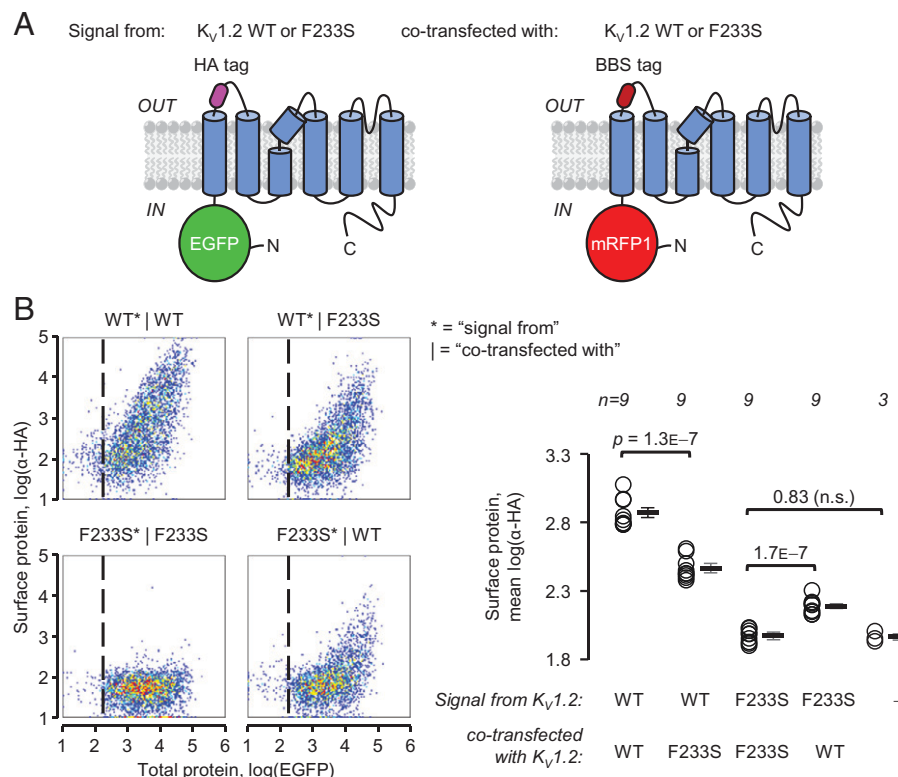


**Fig. 4.**  $K_v1.2(\text{F233S})$  subunits sequester, and are concomitantly rescued by,  $K_v1.2(\text{WT})$ . (A) Constructs used to evaluate  $K_v1.2$  cell-surface trafficking. Each construct emulates one allele.  $K_v1.2$  with N-terminally fused EGFP, reporting total protein production; an extracellular HA tag (as in Fig. 2B) cotransfected with  $K_v1.2$  with N-terminally fused mRFP1, reporting total protein production; and an extracellular bungarotoxin (BTX) binding-site (BBS) tag. (B) Flow cytometry experiments on cells transfected with the constructs in A. The cell-density plots show total protein [ $\log(\text{EGFP})$ ] and surface staining [ $\log(\alpha\text{-HA})$ ] in live cells positive for mRFP1. The vertical dashed lines separate negative (Left) and positive (Right) EGFP cells. Percentage of cells with a positive surface ( $\alpha\text{-HA}$ ) signal (normalized to WT\*|WT, i.e.,  $100 \pm 0.85\%$ ): WT\*|F233S:  $55 \pm 2.0\%$ ; F233S\*|WT:  $22 \pm 1.5\%$ ; F233S\*|F233S:  $1.3 \pm 0.27\%$ . Signals from mRFP1 and BTX in EGFP-positive cells are in *SI Appendix, Fig. S1*. Errors are SEM. n.s. = not significant.

amount of WT RNA constant.  $K_v1.2$  conductance decreased precipitously in a F233S dose-dependent manner (Fig. 5A). In cells with the most F233S cRNA, there was also a  $\sim 5\text{-mV}$  depolarizing shift in voltage dependence (*SI Appendix, Fig. S2 A and B*).

Assuming that F233S does not affect maximal open-probability or single-channel conductance, the data reflect the number of channels on the cell surface. Thus, the data were overlaid with models predicting increasing numbers of F233S subunits participating in trafficking heterotetramers. The model allowing no F233S-containing heterotetramers (black curve) failed to account for the data, predicting too low conductance at high F233S proportions. This is consistent with the observation that F233S subunits are rescued by WT (Fig. 4 and *SI Appendix, Fig. S1*). The green model, allowing one F233S subunit per heterotetramer, described the data best. Models allowing more F233S subunits (cyan and purple curves) greatly overestimated the observed conductance. There was no evidence of cells being overwhelmed by cRNA at the amounts used (*SI Appendix, Fig. S2 C–E*). A thorough discussion of the model assumptions, considering additional simulations and subsequent experimental results, is included in the *SI Appendix*.

The green model suggested that the  $2^{\text{WT}}:2^{\text{F233S}}$  stoichiometry was trafficking deficient. To corroborate this premise, we constructed concatenated  $K_v1.2$  dimers, which are expected to assemble as pseudotetrameric dimers of dimers (29, 30). Accordingly,  $K_v1.2(\text{WT})$ - $K_v1.2(\text{F233S})$  (WT-F233S) dimers exhibited very low conductance ( $\sim 5\%$ ) compared to WT-WT, supporting that the  $2^{\text{WT}}:2^{\text{F233S}}$  stoichiometry is strongly trafficking impaired (Fig. 5B and C). This result independently

excluded the cyan model in Fig. 5A. Despite the very low expression level of WT-F233S channels, it was possible to characterize their voltage dependence: their half-activation potential was shifted ( $\Delta V_{0.5}$ ) by  $22 \pm 0.34\text{ mV}$  compared to WT-WT (Fig. 5D), demonstrating that F233S also impaired  $K_v1.2$  voltage dependence in a dominant-negative manner. The inverted construct F233S-WT had similar properties ( $\Delta V_{0.5}$ :  $25 \pm 0.69\text{ mV}$ ; Fig. 5B–D). F233S-F233S-injected cells did not exhibit current distinguishable from uninjected cells (Fig. 5B and E).

#### The $K_v1.2(\text{F233S})$ Dominant-Negative Trafficking Deficiency Extends to $K_v1.4$ Subunits.

Paralogous potassium channel subunits were shown to assemble into heteromeric channels soon after their cloning (31, 32). In mammals,  $K_v1.4$  subunits are molecular partners of  $K_v1.2$ , forming heterotetrameric channels that contribute to the A current in neurons (3, 5, 6). We used flow cytometry to directly evaluate  $K_v1.2(\text{F233S})$  rescue by  $K_v1.4$  and whether  $K_v1.4$  subunits are sequestered by  $K_v1.2(\text{F233S})$ . COS-7 cells were cotransfected with two constructs:  $K_v1.4$  and  $K_v1.2$  (WT or F233S), each with a different set of fluorescent tags for total and surface protein expression (Fig. 6A).  $K_v1.4$  surface trafficking was reduced in the presence of  $K_v1.2(\text{F233S})$  (Fig. 6B). At the same time,  $K_v1.4$  assisted the trafficking of  $K_v1.2(\text{F233S})$  subunits (Fig. 6C). This represented partial rescue, as the cells did not achieve the same  $K_v1.2$  surface levels as for WT subunits (Fig. 6C).

**$K_v1.4$  and  $K_v1.2(\text{F233S})$  Subunits Likely Form 3:1 and 2:2 Heteromeric Channels.**  $K_v1.4$  subunits are more adept at surface trafficking, both lacking endoplasmic reticulum (ER)



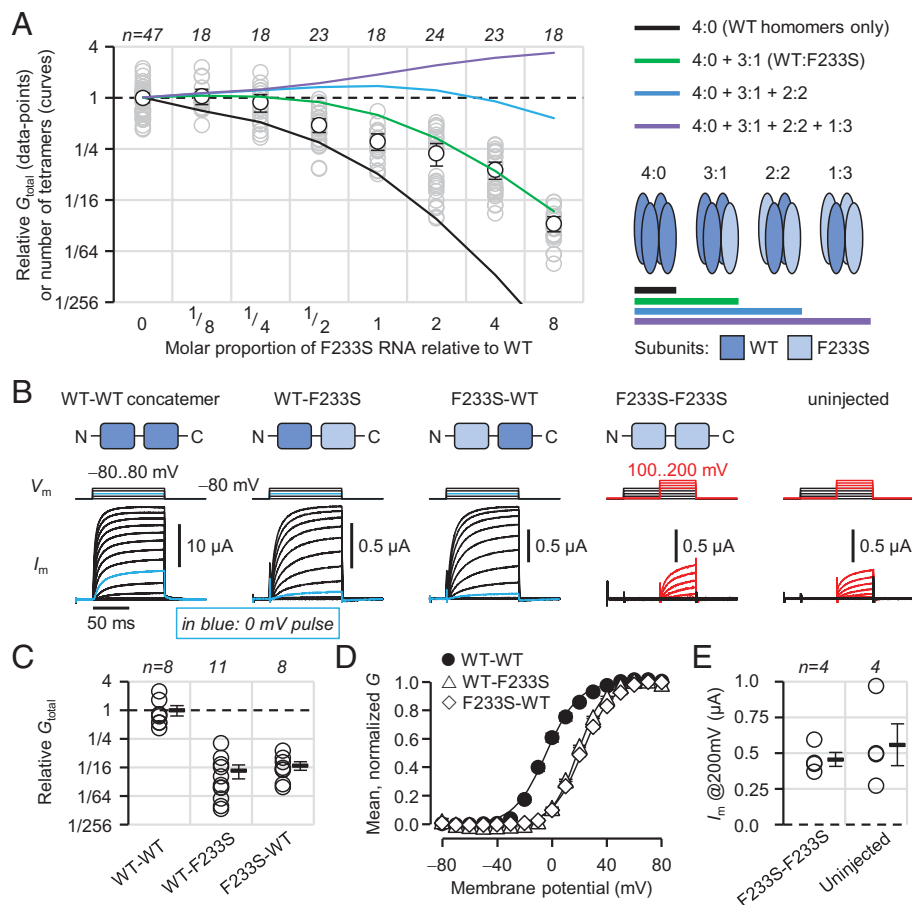


**Fig. 5.** Only 3<sup>WT</sup>:1<sup>F233S</sup> heterotetramers are trafficking capable. (A) Relative conductance in cells injected with  $K_v1.2$ (WT) cRNA and increasing proportion of  $K_v1.2$ (F233S) cRNA. The voltage dependence in all conditions is in *SI Appendix, Fig. S2*. Superimposed curves show number of tetramers of specified composition, relative to the 0-F233S condition, generated by a model assuming binomially distributed tetramerization. (B) Representative COVG current traces from cells injected with dimeric  $K_v1.2$  concatemer cRNA. Relative macroscopic conductance (C) and voltage dependence (D) of cells injected with  $K_v1.2$ (WT)- $K_v1.2$ (WT) (WT-WT) cRNA (relative  $G_{\text{total}} = 1.0 \pm 0.25$ ;  $V_{0.5} = -3.3 \pm 1.5$  mV;  $z_{\text{eff}} = 2.3 \pm 0.16e^0$ ), WT-F233S (relative  $G_{\text{total}} = 0.053 \pm 0.017$ ;  $V_{0.5} = 19 \pm 0.29$  mV;  $z_{\text{eff}} = 2.7 \pm 0.083e^0$ ) or F233S-WT (relative  $G_{\text{total}} = 0.068 \pm 0.014$ ;  $V_{0.5} = 22 \pm 0.59$  mV;  $z_{\text{eff}} = 2.3 \pm 0.10e^0$ ). (E) No current was observed in cells injected with F233S-F233S up to 200 mV (450  $\pm$  48 nA) compared to uninjected cells (560  $\pm$  150 nA;  $P = 0.53$ ). Errors are 95% CI (A) or SEM (B–E).

retention signals and possessing a forward trafficking motif (33–35). In fact, they enhance  $K_v1.2$  trafficking (36). We hypothesized that  $K_v1.4$  is more proficient than  $K_v1.2$ (WT) in rescuing  $K_v1.2$ (F233S). Indeed, in cells expressing  $K_v1.4$ , conductance was significantly decreased only when  $K_v1.2$ (F233S) cRNA was added in eightfold excess (Fig. 7A). Binomial tetramerization models suggested that  $K_v1.4$  homotetramers and 3:1 and 2:2  $K_v1.4$ : $K_v1.2$ (F233S) heterotetramers can traffic (cyan curve), anticipating also some  $K_v1.4$  sequestration (no 1:3 heterotetramers). While  $K_v1.4$  conductance amplitude did not clearly depend on F233S dosage, its voltage dependence did, exhibiting a progressive shift to more depolarized potentials with increasing F233S (Fig. 7B and C and *SI Appendix, Fig. S3*) and supporting that  $K_v1.4$ : $K_v1.2$ (F233S) heterotetramers can traffic in oocytes. Note also the spontaneous decrease in current during depolarization (Fig. 7C) caused by an N-terminal inactivation motif blocking the channel pore (37, 38).

As before, we used dimeric concatemers to evaluate the trafficking and biophysical properties of the 2:2  $K_v1.4$ : $K_v1.2$  stoichiometry.  $K_v1.4$ - $K_v1.2$ (F233S) constructs exhibited full conductance compared with  $K_v1.4$ - $K_v1.2$ (WT) ( $P = 0.76$ ; Fig. 7D and E), supporting that the 2:2  $K_v1.4$ : $K_v1.2$ (F233S) stoichiometry is trafficking capable. However, the inverted construct,  $K_v1.2$ (F233S)- $K_v1.4$ , exhibited strongly diminished conductance (Fig. 7D and F). The significance of this result for the mechanism of F233S-caused trafficking impairment is discussed below. Both

$K_v1.2$ (F233S)-containing constructs exhibited right-shifted voltage dependence compared to their WT counterparts (Fig. 7G). Finally, our constructs with a C-terminal  $K_v1.4$  lacked fast inactivation (Fig. 7D). Since the inactivation particle is located at the  $K_v1.4$  N terminus (37, 38), perhaps it cannot block the channel when N-terminally tethered.

**Operation of the  $K_v1.2$ (F233S) VSD.** We exploited the rescue of  $K_v1.2$ (F233S) subunits by WT  $K_v1.2$  and  $K_v1.4$  to investigate the function of the F233S-bearing VSD. To selectively track the activation of F233S-bearing subunits, we used voltage-clamp fluorometry (VCF) (39, 40). In this approach, a Cys is substituted at a position expected to undergo conformational changes [A291C, at the extracellular flank of  $K_v1.2$  S4 (8, 41)]. The Cys is then labeled with a thiol-reactive, environment-sensitive fluorophore, such as MTS-TAMRA. Thus, changes in ensemble fluorescence ( $\Delta F$ ) report VSD activation transitions.  $K_v1.2$ (A291C) channels showed robust downward  $\Delta F$  signals (Fig. 8A), reporting VSD activation upon membrane depolarization and its rapid deactivation upon repolarization. By only incorporating the A291C substitution in F233S-bearing subunits, only the movements of F233S-containing VSDs are optically reported; the VSDs of rescuing  $K_v1.2$  and  $K_v1.4$  subunits also undergo voltage-dependent movements, but they are not fluorescently labeled and therefore their movements are not optically reported (*SI Appendix, Fig. S4*). These experiments revealed that the rescued  $K_v1.2$ (F233S) VSD

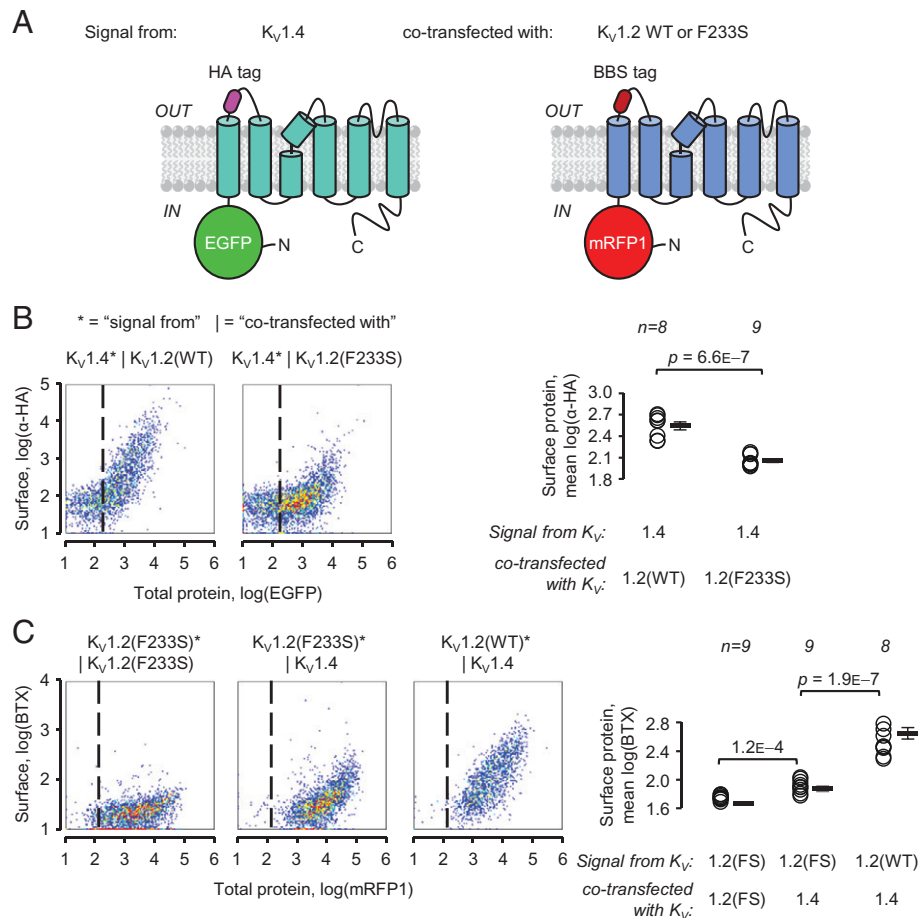


**Fig. 6.**  $K_v1.2$ (F233S) subunits concomitantly suppress and are rescued by  $K_v1.4$ . (A) Constructs used to evaluate  $K_v1.2$  and  $K_v1.4$  cell-surface trafficking.  $K_v1.4$  with N-terminally fused EGFP, reporting total protein production; an extracellular HA tag cotransfected with  $K_v1.2$  with N-terminally fused mRFP1, reporting total protein production; and an extracellular BBS tag. (B) Flow cytometry experiments on cells transfected with constructs in A. The cell-density plots show total protein [log(EGFP)] and surface staining [log( $\alpha$ -HA)] in live cells positive for mRFP1. The vertical dashed line separates negative (Left) and positive (Right) EGFP. Percentage of cells with a positive surface ( $\alpha$ -HA) signal [normalized to  $K_v1.4$ \*| $K_v1.2$ (WT), i.e.,  $100 \pm 2.4\%$ ]:  $K_v1.4$ \*| $K_v1.2$ (F233S):  $8.5 \pm 1.9\%$ . (C) As in B, showing the signals from  $K_v1.2$  constructs cotransfected with  $K_v1.4$ . Plots of log(mRFP1) (total protein) against log(BTX) (cell-surface expression). The vertical dashed line separates negative (Left) and positive (Right) mRFP1 cells among the plotted live, EGFP-positive cells. Percentage of cells with a positive surface (BTX) signal [normalized to  $K_v1.2$ (WT)\*| $K_v1.4$ , i.e.,  $100 \pm 2.7\%$ ]:  $K_v1.2$ (F233S)\*| $K_v1.2$ (F233S):  $3.7 \pm 0.36\%$ ;  $K_v1.2$ (F233S)\*| $K_v1.4$ :  $16 \pm 3.1\%$ . Errors are SEM.

activates with a modestly affected voltage dependence, as well as near-normal valence and activation kinetics (Fig. 8 A–D).

$K_v1.4$  subunits confer a particular advantage to this experimental paradigm, enabling the direct observation of VSD-pore coupling. Their unique (in the  $K_v1$  family) N-terminal inactivation particle binds to, and blocks, the open pore (N-type inactivation, Fig. 7C) (37). In doing so, the inactivation particle prevents pore closure (42, 43), which in turn impedes the return of the VSD to its resting conformation. This phenomenon, termed off-charge immobilization, persists until the inactivation particle dissociates and the pore closes. It is experimentally observable in gating-current (44, 45) and optical (46) experiments.

Accordingly, in the presence of  $K_v1.4$  subunits, and at depolarizations that evoked pore opening (and N-type inactivation),  $K_v1.2$ (F233S) VSD deactivation was markedly slower (Fig. 8C), consistent with off-charge immobilization. This indicates that the rescued  $K_v1.2$ (F233S) VSDs were functionally coupled to the state of the channel pore (Fig. 8 E and F). When  $K_v1.2$ (F233S) subunits were rescued by  $K_v1.4$  lacking an inactivation particle, their VSD deactivated quickly (SI Appendix, Fig. S4).

## Discussion

In this work, we report on a *KCNA2* variant discovered in a male child with epilepsy (Fig. 1 C and D). The protein product of

*KCNA2*,  $K_v1.2$  subunits of voltage-gated potassium channels are expressed throughout the brain as homotetrameric channels (Fig. 1A) or participating in heterotetrameric complexes with other  $K_v1$  channel subunits (47), where they regulate neuronal excitability and synaptic release. The *KCNA2* variant studied here results in the substitution of a residue (F233S) at the core of the bundle of transmembrane helices comprising the channel VSD (Fig. 1B). This mutation completely abolished the surface trafficking of  $K_v1.2$ (F233S) subunits (Fig. 2). We also discovered that the mutant subunits are dominant negative, suppressing the surface trafficking of their WT allele (Figs. 3 and 4 and SI Appendix, Fig. S1) but also  $K_v1.4$ , a known molecular partner of  $K_v1.2$  (Fig. 6). Yet the severe trafficking defect of  $K_v1.2$ (F233S) subunits was ameliorated in the presence of WT  $K_v1.2$  and  $K_v1.4$  subunits, demonstrated by both surface labeling (Figs. 4 and 6 and SI Appendix, Fig. S1) and electrophysiological evidence (Figs. 5 and 7). This allowed the direct observation of the mutant VSD activation (Fig. 8 and SI Appendix, Fig. S4). Our work classifies this previously unreported *KCNA2* variant as a dominant-negative mutation that leads to loss of  $K_v1.2$  channel function as a phenotype and could also decrease the function of other  $K_v1$ -family molecular partners.

**How Does F233S Affect  $K_v1.2$  Functional Properties?** F233 has an eminent role in voltage sensing as the charge transfer center (Fig.

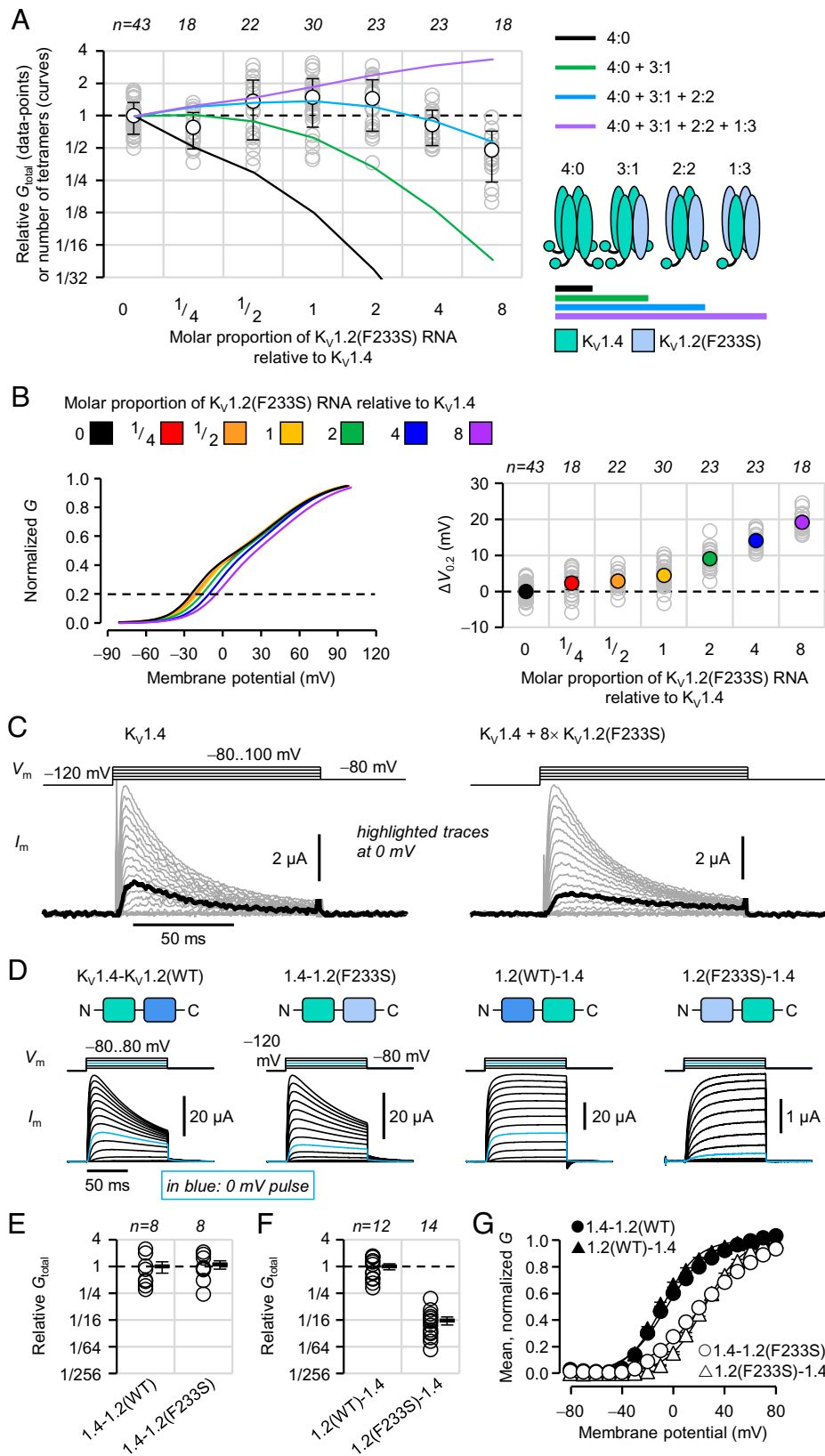


**Fig. 7.**  $K_v1.4$  and  $K_v1.2(\text{F233S})$  subunits form 3:1 and 2:2 heteromeric channels. (A) Relative peak conductance in cells injected with  $K_v1.4$  cRNA and increasing molar proportion of  $K_v1.2(\text{F233S})$  cRNA. Superimposed curves show the number of tetramers of specified composition relative to the 0-F233S condition, generated by a model assuming binomially distributed tetramerization. (B) Fitted Boltzmann distributions of peak macroscopic conductance from the same cells as in A. Data, parameters, and individual curves in *SI Appendix, Fig. S3*. The potential of 20% activation ( $V_{0.2}$ ) best shows the F233S-dependent shift in voltage dependence on the right. Error bars are  $\pm 95\%$  CI. (C) Representative TEVC current traces demonstrate altered voltage-dependent properties in heteromeric channels. (D) Representative COVG current traces from cells injected with dimeric  $K_v1.4/K_v1.2$  concatemer cRNA. Relative macroscopic conductance (E and F) and voltage dependence (G) of cells injected with 1.4-1.2(WT) (relative  $G_{\text{total}} = 1.0 \pm 0.29$ ;  $V_{0.5} = -4.8 \pm 1.3$  mV;  $z_{\text{eff}} = 1.6 \pm 0.038$  e $^0$ ); 1.4-1.2(F233S) (relative  $G_{\text{total}} = 1.1 \pm 0.23$ ;  $V_{0.5} = 23 \pm 1.2$  mV;  $z_{\text{eff}} = 1.2 \pm 0.027$  e $^0$ ); 1.2(WT)-1.4 (relative  $G_{\text{total}} = 1.0 \pm 0.15$ ;  $V_{0.5} = -8.2 \pm 0.95$  mV;  $z_{\text{eff}} = 1.9 \pm 0.12$  e $^0$ ); 1.2(F233S)-1.4 (relative  $G_{\text{total}} = 0.062 \pm 0.012$ ;  $V_{0.5} = 24 \pm 1.2$  mV;  $z_{\text{eff}} = 1.8 \pm 0.044$  e $^0$ ). Conductance for 1.4-1.2 constructs, which exhibit fast inactivation, was calculated at peak current. Errors are SEM.



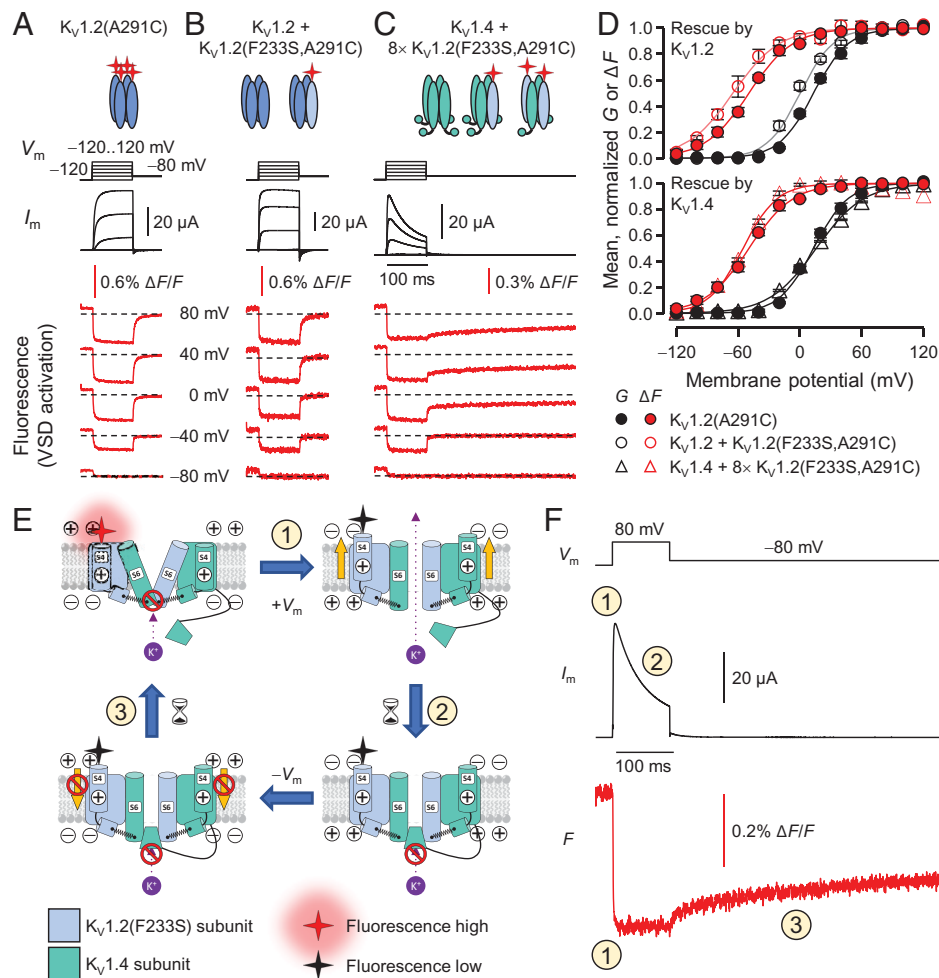


**Fig. 8.** Operation of the  $K_v1.2(F233S)$  VSD. (A) VCF experiments on  $K_v1.2$  homotetramers, fluorescently labeled outside the S4 helix (A291C) to optically track the voltage-dependent activation of the VSD (Fig. 1B).  $V_m$ ,  $I_m$  (black), and simultaneously acquired fluorescence deflections ( $\Delta F$ , red). VSD activation causes fluorophore quenching, reported as negative  $\Delta F$  (8). (B and C) As in A, but the fluorescence label is in  $K_v1.2(F233S)$  subunits rescued by WT  $K_v1.2$  (B) or  $K_v1.4$  (C). Note that VSD deactivation is delayed in C (interpreted below). (D) Normalized macroscopic conductance ( $G$ , black) and VSD activation ( $\Delta F$ , red), fit to Boltzmann distributions.  $K_v1.2(A291C)$   $G$ :  $V_{0.5} = 14 \pm 2.8$  mV,  $z_{eff} = 1.6 \pm 0.14$   $e^0$ ;  $\Delta F$ :  $V_{0.5} = -50 \pm 1.8$  mV,  $z_{eff} = 1.3 \pm 0.22$   $e^0$ ;  $n = 4$ .  $K_v1.2/1.2(F233S, A291C)$   $G$ :  $V_{0.5} = -0.89 \pm 2.4$  mV,  $z_{eff} = 1.6 \pm 0.074$   $e^0$ ;  $\Delta F$ :  $V_{0.5} = -64 \pm 4.0$  mV,  $z_{eff} = 1.2 \pm 0.11$   $e^0$ ;  $n = 6$ .  $K_v1.4/1.2(F233S, A291C)$   $G$ :  $V_{0.5} = 16 \pm 0.75$  mV,  $z_{eff} = 1.1 \pm 0.039$   $e^0$ ;  $\Delta F$ :  $V_{0.5} = -56 \pm 1.0$  mV,  $z_{eff} = 1.6 \pm 0.13$   $e^0$ ;  $n = 6$ . Errors are SEM. Note that the  $K_v1.2(A291C)$  conductance (black filled circles) is right shifted by  $\sim 15$  mV compared to WT due to the A291C mutation (8); the  $K_v1.2/1.2(F233S, A291C)$  conductance (black open circles) has a large contribution from WT homotetramers, so it is relatively left shifted. (E and F) Interpretation of data from  $K_v1.4/1.2(F233S, A291C)$  heterotetramers (C). The diagrams in E show pore and VSD states in a hypothetical  $K_v1.4/1.2(F233S, A291C)$  heterotetramer (only two subunits shown). Numbered transitions are registered on the exemplary current and fluorescence traces in F. (E) *Top Left*: The  $V_m$  is negative; the VSDs are resting (label in high-fluorescence state), and the pore is closed (no current). Upon depolarization (transition 1) VSDs activate and the channel opens (*Top Right*), reported as current onset and downward  $\Delta F$  in F. Next (transition 2),  $K_v1.4$  inactivation particles block the channels (*Bottom Right*), reported as current reduction. Following membrane repolarization, the inactivation particle persists in the pore, preventing its closure (*Bottom Left*). It takes time for the particle to dissociate (transition 3), delaying VSD deactivation (off-charge immobilization), reported as slow  $\Delta F$  recovery. In the absence of an inactivation particle, the VSD deactivates with fast kinetics (*SI Appendix, Fig. S4B*).

1B) (11). How does its substitution affect channel function? Since  $K_v1.2(F233S)$  homotetramers could not traffic (Fig. 2), it was not possible to directly determine their voltage dependence. In the Shaker  $K^+$  channel, the archetype for functional  $K_v$  studies, some VSD mutations have been shown to perturb voltage dependence proportionally to the number of affected subunits (29, 48).  $K_v1.2(WT/F233S)$  concatemers, which represent the  $2^{WT:F233S}$  stoichiometry, exhibit a depolarizing shift ( $\Delta V_{0.5}$ ) of 24 mV, so we may infer that  $K_v1.2(F233S)$  homotetramers would exhibit a 48-mV shift. The equivalent mutation in Shaker(F290S) induced a stronger  $\Delta V_{0.5}$  of  $\sim 80$  mV (11).

The four VSDs in a  $K_v$  channel are thought to activate independently by membrane depolarization (early transitions) and then undergo a concerted late transition that leads to pore opening (49). In Shaker, mutations that disrupt VSD-pore coupling result in depolarizing shifts of late VSD transitions and pore opening (49), an effect recapitulated by F290S (13). This

was not observed in the VSD of  $K_v1.2(F233S)$  (Fig. 8D), while off-charge immobilization (in the presence of  $K_v1.4$ ) strongly indicates functional VSD-pore coupling (Fig. 8 and *SI Appendix, Fig. S4*). However, the requisite association of  $K_v1.2(F233S)$  with rescuer subunits may have rectified its late VSD transitions, occurring in concert with the movements of WT VSDs in the heterotetrameric channels.

Our view is that charge-transfer-center disruption has similar effects on the two channels, albeit milder in  $K_v1.2$ . Previous work indicates that  $K_v1.2$  has a thicker hydrophobic septum than Shaker (12), perhaps rendering its VSD more resilient to charge-transfer-center disruption.

**Mechanism of F233S-Mediated Trafficking Impairment.** Why does the cellular protein biosynthesis and secretory machinery prevent  $K_v1.2(F233S)$ -subunit expression? We propose that the F233S mutation hinders trafficking at two distinct stages:

“early” and “late”. The former likely include processes such as translation, helix formation, and translocation, thought to occur early in channel biosynthesis (50). The latter likely involve the trafficking of translocated subunits and their interaction with ER proteins.

Starting with the  $K_{V1.4}/K_{V1.2}(F233S)$  concatemer experiments, the construct with an N-terminal  $K_{V1.4}$  subunit is trafficking capable, whereas the construct with an N-terminal  $K_{V1.2}(F233S)$  is trafficking impaired (Fig. 7 *D–F*). The only difference between the two is the order in which the two domains are synthesized and introduced to the cell secretory pathway. In related  $K_{V1.3}$  channels, helix S2 functions as the signal for translocation and establishment of N terminus topology (51).  $K_{V1.3}$  S2 helix formation depends on the presence of a WF motif in the middle of the helix (W232 and F233 in  $K_{V1.2}$ ) that prevents premature S2 helical formation (52). As this motif is highly conserved across  $K_V$  channel subfamilies, its helical-suppressor function is likely crucial to translocation and could be a major first impediment for the functional expression of N-terminal  $K_{V1.2}(F233S)$  peptides, whether they are monomers (Fig. 2) or concatenated with WT  $K_{V1.2}$  (Fig. 5 *B* and *C*) or  $K_{V1.4}$  (Fig. 7 *D* and *F*). Aberrant  $K_{V1.2}(F233S)$  translocation may in turn interfere with other processes important for trafficking, such as electrostatic interactions within the VSD (53) or glycosylation at the S1–S2 linker (54, 55).

By contrast, when  $K_{V1.2}(F233S)$  is the C-terminal partner of  $K_{V1.4}$ , trafficking is not affected (Fig. 7 *D* and *E*). In this construct, the N-terminal  $K_{V1.4}$  likely undergoes a successful translocation first. Why does the C-terminal  $K_{V1.2}(F233S)$  not oppose translocation? We suggest that this is evidence of cooperative translocation. It is possible that such a mechanism (a capable N-terminal partner assisting the translocation of downstream domains) is employed by natural concatemers, such as two-pore channels and pseudotetrameric voltage-gated calcium and sodium channels (56).

Why does N-terminal WT  $K_{V1.2}$ , then, not facilitate the trafficking of C-terminal  $K_{V1.2}(F233S)$  (Fig. 5 *B* and *O*)? Likely it does, but trafficking is then halted by later events, unrelated to biosynthesis, folding, and translocation. These may include posttranslational modification and interaction with the ER protein quality-control apparatus.  $K_{V1.2}$  subunits have ER retention motifs which  $K_{V1.4}$  lack; additionally,  $K_{V1.4}$  possess forward trafficking signals (33–35). These elements could underlie the successful trafficking of 3:1 and 2:2  $K_{V1.4}/K_{V1.2}(F233S)$  heterotetramers and  $K_{V1.4}-K_{V1.2}(F233S)$  concatemers, but not 2:2  $K_{V1.2}(WT)/K_{V1.2}(F233S)$  heterotetramers or the  $K_{V1.2}(WT-F233S)$  concatemers. It appears that inclusion of trafficking-deficient  $K_{V1.2}(F233S)$  subunits in heterotetramers imposes a quantal trafficking penalty, abated by trafficking-enhancing elements, as in  $K_{V1.4}$ .

In conclusion, we propose this model for  $K_{V1.2}(F233S)$ -subunit trafficking: Nascent peptides tetramerize early (28), assembling into homo- and heterotetramers.  $K_{V1.2}(F233S)$  homotetramers are immediately excluded, encountering an early translocation impediment and receiving no assistance from WT partner subunits. This early block may also prevent heterotetramers with three  $K_{V1.2}(F233S)$  subunits from trafficking; alternatively, these are blocked later in the ER. Heterotetramers with two  $K_{V1.2}(F233S)$  translocate successfully but then have different fates, depending on the trafficking adeptness of their partner subunits: those with  $K_{V1.2}$  are blocked (Fig. 5), whereas those with  $K_{V1.4}$  traffic successfully (Fig. 7).

By comparison, Shaker(F290S) channels were reported to have “medium current level” (11) and sufficient expression for the measurement of gating currents (13). We find it interesting that while

the effects of F→S are similar in the two channels, their severities are inverted: strong functional impairment and modest trafficking deficiency in Shaker, and vice versa for  $K_{V1.2}$ . This disparity indicates that the trafficking and functional defects are not strictly linked. Since F233/F290 is critical for two altogether different functions—S2-helix formation and translocation of the nascent polypeptide (52) and voltage sensing in the mature protein (11, 13)—these could be differentially modified by other parts of the  $K_{V1.2}$  and Shaker channels.

There is still much to discover about the identity of early and late events of  $K_{V1.2}(F233S)$  trafficking impairment. We are certain that this variant, serendipitously discovered in an epilepsy patient, can serve as a tool to investigate the fundamental aspects of channel biogenesis, trafficking, and oligomerization.

**Neuronal Consequences of a Dominant-Negative *KCNA2* Variant.** The ability of  $K_V$  subunits to form heteromeric channels is a major source of conductance diversity in the brain. However, it can act as a double-edged sword, as trafficking deficiencies in one gene can have multigenic dominant-negative effects. As the two somatic *KCNA2* alleles are presumably under the same transcriptional control, our experiments suggest that the neurons of the heterozygote patient will have ~20%  $K_{V1.2}$  conductance (Fig. 3 *A* and *B*). Effects on other subunits will depend on their relative expression levels. We posit that epileptogenesis is mainly driven by  $K_{V1.2}$  loss of function, with some  $K_{V1.4}$  decrease in neurons where these genes are coexpressed.  $K_{V1.1}$  are also likely suppressed by  $K_{V1.2}(F233S)$ , as they traffic less proficiently than  $K_{V1.2}$  or  $K_{V1.4}$  due to their potent ER retention signal (35). Loss of  $K_{V1.2}$  function should prolong action potentials in both excitatory and inhibitory neurons. In the former, this can cause increased synaptic release (4). On the other hand, fast-gating  $K_{V3}$  channels are more abundant in inhibitory neurons (57–59), where they delimit action potential duration (60, 61); thus, some inhibitory synaptic release is protected from loss of  $K_{V1.2}$ . The resulting imbalance of excitatory and inhibitory signals could veer neuronal circuits toward epilepsy (62).

## Methods

This study was reviewed and deemed exempt by the Children’s Hospital Los Angeles Institutional Review Board. A consent form by Children’s Hospital Los Angeles compliant with the Health Insurance Portability and Accountability Act of 1996 (HIPAA) was signed by the patient’s parents. DNA was extracted from the peripheral blood of the patient and each of his unaffected parents as comparators using a commercially available kit (Promega Maxwell RSC DNA Extraction Kit). Original trafficking-assay and  $K_{V1.4}$  plasmids were described in (27) and (63), respectively. Confocal microscopy, cut-open oocyte Vaseline gap (64), and VCF (65) experiments were performed as previously described (8). For some flow cytometry experiments, the methodology [previously described in Pantazis et al. (8)] was expanded to four colors to evaluate synthesis and surface trafficking of two constructs simultaneously. Two-electrode voltage-clamp (TEVC) experiments were performed in an OpusXpress 6000A (Axon Instruments) parallel voltage clamp to facilitate testing of a large number of cells.

**Data Availability.** All study data are included in the article and/or *SI Appendix*.

**ACKNOWLEDGMENTS.** This work was supported by start-up funds by the Wallenberg Center for Molecular Medicine at Linköping University (Knut and Alice Wallenberg Foundation) and Vetenskapsrådet (Swedish Research Council) research grant VR-MH 2019-00988 (A.P.); Center for Systems Neurobiology stipend support, Linköping University (K.W.); NIH National Institute of General Medical Sciences grant R35GM131896 (R.O.); David Geffen School of Medicine Precision Medicine Seed Grant (M.O. and R.O.); and NIH National Heart, Lung,

and Blood Institute grant HL152296 (M.O.). We are grateful to Benoît Roux, Lily Y. Jan, and James S. Trimmer for their generous gifts of  $K_v1.2$  and  $K_v1.4$  constructs. We thank Gordana Raca, Cindy Fong, David Ruble, and Moiz Bootwalla for technical assistance with genetic testing. Confocal imaging and flow cytometry were performed using instrumentation at Linköping University Microscopy and Flow Cytometry cores, respectively: we thank Vesa Loitto and Mikael Pihl for expert consultation. The OpusXpress 6000A was a gift from the German Institute of Human Nutrition, Potsdam-Rehbrücke, to Fredrik Elinder, and it was set up by Johan Brask; we are grateful to both for its use.

Author affiliations: <sup>a</sup>Division of Neurobiology, Department of Biomedical and Clinical Sciences (BKV), Linköping University, 581 83 Linköping, Sweden; <sup>b</sup>Center for Personalized Medicine, Children's Hospital Los Angeles, Los Angeles, CA 90027; <sup>c</sup>Division of Genomic Medicine, Department of Pathology, Children's Hospital Los Angeles, Los Angeles, CA 90027; <sup>d</sup>Division of Molecular Medicine, Department of Anesthesiology & Perioperative Medicine, David Geffen School of Medicine, University of California, Los Angeles, CA 90095; <sup>e</sup>Comprehensive Epilepsy Program, Children's Hospital Los Angeles, Los Angeles, CA 90027; <sup>f</sup>UCLA Cardiovascular Theme, David Geffen School of Medicine, University of California, Los Angeles, CA 90095; <sup>g</sup>Brain Research Institute, David Geffen School of Medicine, University of California, Los Angeles, CA 90095; <sup>h</sup>Department of Physiology, David Geffen School of Medicine, University of California, Los Angeles, CA 90095; and <sup>i</sup>Wallenberg Center for Molecular Medicine, Linköping University, 581 83 Linköping, Sweden

1. W. Stühmer *et al.*, Molecular basis of functional diversity of voltage-gated potassium channels in mammalian brain. *EMBO J.* **8**, 3235–3244 (1989).
2. J. S. Trimmer, Subcellular localization of  $K^+$  channels in mammalian brain neurons: Remarkable precision in the midst of extraordinary complexity. *Neuron* **85**, 238–256 (2015).
3. B. P. Bean, The action potential in mammalian central neurons. *Nat. Rev. Neurosci.* **8**, 451–465 (2007).
4. M. H. Kole, J. J. Letzkus, G. J. Stuart, Axon initial segment  $K_v1$  channels control axonal action potential waveform and synaptic efficacy. *Neuron* **55**, 633–647 (2007).
5. M. Sheng, Y. J. Liao, Y. N. Jan, L. Y. Jan, Presynaptic A-current based on heteromultimeric  $K^+$  channels detected in vivo. *Nature* **365**, 72–75 (1993).
6. S. K. Coleman, J. Newcombe, J. Pryke, J. O. Dolly, Subunit composition of  $K_v1$  channels in human CNS. *J. Neurochem.* **73**, 849–858 (1999).
7. S. Masnada *et al.*, Clinical spectrum and genotype-phenotype associations of KCNA2-related encephalopathies. *Brain* **140**, 2337–2354 (2017).
8. A. Pantazis *et al.*, Tracking the motion of the  $K_v1.2$  voltage sensor reveals the molecular perturbations caused by a de novo mutation in a case of epilepsy. *J. Physiol.* **598**, 5245–5269 (2020).
9. J. H. Döring *et al.*, Refining genotypes and phenotypes in KCNA2-related neurological disorders. *Int. J. Mol. Sci.* **22**, 2824 (2021).
10. P. Imbrici *et al.*, A Novel KCNA2 Variant in a Patient with Non-Progressive Congenital Ataxia and Epilepsy: Functional Characterization and Sensitivity to 4-Aminopyridine. *Int. J. Mol. Sci.* **22**, 9913 (2021).
11. X. Tao, A. Lee, W. Limapichat, D. A. Dougherty, R. MacKinnon, A gating charge transfer center in voltage sensors. *Science* **328**, 67–73 (2010).
12. I. G. Ishida, G. E. Rangel-Yescas, J. Carrasco-Zanini, L. D. Islas, Voltage-dependent gating and gating charge measurements in the  $K_v1.2$  potassium channel. *J. Gen. Physiol.* **145**, 345–358 (2015).
13. J. J. Lacroix, F. Bezanilla, Control of a final gating charge transition by a hydrophobic residue in the S2 segment of a  $K^+$  channel voltage sensor. *Proc. Natl. Acad. Sci. U.S.A.* **108**, 6444–6449 (2011).
14. T. Kalstrup, R. Blunck, S4-S5 linker movement during activation and inactivation in voltage-gated  $K^+$  channels. *Proc. Natl. Acad. Sci. U.S.A.* **115**, E6751–E6759 (2018).
15. F. Tombola, M. M. Pathak, E. Y. Isacoff, How does voltage open an ion channel? *Annu. Rev. Cell Dev. Biol.* **22**, 23–52 (2006).
16. S. I. Björkesson, F. Elinder, Structure, function, and modification of the voltage sensor in voltage-gated ion channels. *Cell Biochem. Biophys.* **52**, 149–174 (2008).
17. B. Chanda, F. Bezanilla, A common pathway for charge transport through voltage-sensing domains. *Neuron* **57**, 345–351 (2008).
18. R. Blunck, Z. Batulan, Mechanism of electromechanical coupling in voltage-gated potassium channels. *Front. Pharmacol.* **3**, 166 (2012).
19. M. O. Jensen *et al.*, Mechanism of voltage gating in potassium channels. *Science* **336**, 229–233 (2012).
20. C. S. Swaiger, S. I. Liin, F. Elinder, E. Lindahl, The conserved phenylalanine in the  $K^+$  channel voltage-sensor domain creates a barrier with unidirectional effects. *Biophys. J.* **104**, 75–84 (2013).
21. S. B. Long, X. Tao, E. B. Campbell, R. MacKinnon, Atomic structure of a voltage-dependent  $K^+$  channel in a lipid membrane-like environment. *Nature* **450**, 376–382 (2007).
22. M. Lek *et al.*, Exome Aggregation Consortium, Analysis of protein-coding genetic variation in 60,706 humans. *Nature* **536**, 285–291 (2016).
23. M. J. Landrum *et al.*, ClinVar: Improving access to variant interpretations and supporting evidence. *Nucleic Acids Res.* **46**, D1062–D1067 (2018).
24. P. D. Stenson *et al.*, The Human Gene Mutation Database: Towards a comprehensive repository of inherited mutation data for medical research, genetic diagnosis and next-generation sequencing studies. *Hum. Genet.* **136**, 665–677 (2017).
25. N. L. Sim *et al.*, SIFT web server: Predicting effects of amino acid substitutions on proteins. *Nucleic Acids Res.* **40**, W452–W457 (2012).
26. J. M. Schwarz, D. N. Cooper, M. Schuelke, D. Seelow, MutationTaster2: Mutation prediction for the deep-sequencing age. *Nat. Methods* **11**, 361–362 (2014).
27. C. Gu, Y. N. Jan, L. Y. Jan, A conserved domain in axonal targeting of  $K_v1$  (Shaker) voltage-gated potassium channels. *Science* **301**, 646–649 (2003).
28. J. Lu, J. M. Robinson, D. Edwards, C. Deutsch, T1-T1 interactions occur in ER membranes while nascent Kv peptides are still attached to ribosomes. *Biochemistry* **40**, 10934–10946 (2001).
29. E. R. Liman, J. Tytgat, P. Hess, Subunit stoichiometry of a mammalian  $K^+$  channel determined by construction of multimeric cDNAs. *Neuron* **9**, 861–871 (1992).
30. S. Akhtar, O. Shamotienko, M. Papakosta, F. Ali, J. O. Dolly, Characteristics of brain  $K_v1$  channels tailored to mimic native counterparts by tandem linkage of alpha subunits: Implications for  $K^+$  channelopathies. *J. Biol. Chem.* **277**, 16376–16382 (2002).
31. E. Y. Isacoff, Y. N. Jan, L. Y. Jan, Evidence for the formation of heteromultimeric potassium channels in *Xenopus* oocytes. *Nature* **345**, 530–534 (1990).
32. J. P. Ruppersberg *et al.*, Heteromultimeric channels formed by rat brain potassium-channel proteins. *Nature* **345**, 535–537 (1990).
33. H. Misonou, J. S. Trimmer, Determinants of voltage-gated potassium channel surface expression and localization in Mammalian neurons. *Crit. Rev. Biochem. Mol. Biol.* **39**, 125–145 (2004).
34. D. Li, K. Takimoto, E. S. Levitan, Surface expression of  $K_v1$  channels is governed by a C-terminal motif. *J. Biol. Chem.* **275**, 11597–11602 (2000).
35. L. N. Manganas *et al.*, Identification of a trafficking determinant localized to the  $K_v1$  potassium channel pore. *Proc. Natl. Acad. Sci. U.S.A.* **98**, 14055–14059 (2001).
36. L. N. Manganas, J. S. Trimmer, Subunit composition determines  $K_v1$  potassium channel surface expression. *J. Biol. Chem.* **275**, 29685–29693 (2000).
37. J. Tseng-Crank, J. A. Yao, M. F. Berman, G. N. Tseng, Functional role of the NH2-terminal cytoplasmic domain of a mammalian A-type K channel. *J. Gen. Physiol.* **102**, 1057–1083 (1993).
38. Si. Kondoh, K. Ishii, Y. Nakamura, N. Taira, A mammalian transient type  $K^+$  channel, rat  $K_v1.4$ , has two potential domains that could produce rapid inactivation. *J. Biol. Chem.* **272**, 19333–19338 (1997).
39. L. M. Mannuzzu, M. M. Moronne, E. Y. Isacoff, Direct physical measure of conformational rearrangement underlying potassium channel gating. *Science* **271**, 213–216 (1996).
40. M. Priest, F. Bezanilla, Functional site-directed fluorimetry. *Adv. Exp. Med. Biol.* **869**, 55–76 (2015).
41. A. J. Horne, C. J. Peters, T. W. Claydon, D. Fedida, Fast and slow voltage sensor rearrangements during activation gating in  $K_v1.2$  channels detected using tetramethylrhodamine fluorescence. *J. Gen. Physiol.* **136**, 83–99 (2010).
42. S. D. Demo, G. Yellen, The inactivation gate of the Shaker  $K^+$  channel behaves like an open-channel blocker. *Neuron* **7**, 743–753 (1991).
43. J. P. Ruppersberg, R. Frank, O. Pongs, M. Stocker, Cloned neuronal IK(A) channels reopen during recovery from inactivation. *Nature* **353**, 657–660 (1991).
44. C. M. Armstrong, F. Bezanilla, Inactivation of the sodium channel. II. Gating current experiments. *J. Gen. Physiol.* **70**, 567–590 (1977).
45. M. J. Roux, R. Olcese, L. Toro, F. Bezanilla, E. Stefani, Fast inactivation in Shaker  $K^+$  channels. Properties of ionic and gating currents. *J. Gen. Physiol.* **111**, 625–638 (1998).
46. N. Savalli, A. Kondratiev, S. B. de Quintana, L. Toro, R. Olcese, Modes of operation of the BKCa channel beta2 subunit. *J. Gen. Physiol.* **130**, 117–131 (2007).
47. J. Xu, W. Yu, Y. N. Jan, L. Y. Jan, M. Li, Assembly of voltage-gated potassium channels. Conserved hydrophilic motifs determine subfamily-specific interactions between the alpha-subunits. *J. Biol. Chem.* **270**, 24761–24768 (1995).
48. D. G. Gagnon, F. Bezanilla, The contribution of individual subunits to the coupling of the voltage sensor to pore opening in Shaker K channels: Effect of ILT mutations in heterotetramers. *J. Gen. Physiol.* **136**, 555–568 (2010).
49. J. L. Ledwell, R. W. Aldrich, Mutations in the S4 region isolate the final voltage-dependent cooperative step in potassium channel activation. *J. Gen. Physiol.* **113**, 389–414 (1999).
50. C. Deutsch, Potassium channel ontogeny. *Annu. Rev. Physiol.* **64**, 19–46 (2002).
51. L. Tu, J. Wang, A. Helm, W. R. Skach, C. Deutsch, Transmembrane biogenesis of  $K_v1.3$ . *Biochemistry* **39**, 824–836 (2000).
52. L. Tu, C. Deutsch, Determinants of helix formation for a  $K_v1.3$  transmembrane segment inside the ribosome exit tunnel. *J. Mol. Biol.* **429**, 1722–1732 (2017).
53. S. K. Tiwari-Woodruff, C. T. Schulteis, A. F. Mock, D. M. Papazian, Electrostatic interactions between transmembrane segments mediate folding of Shaker  $K^+$  channel subunits. *Biophys. J.* **72**, 1489–1500 (1997).
54. J. Zhu *et al.*, The  $K_v1.2$  potassium channel: The position of an N-glycan on the extracellular linkers affects its protein expression and function. *Brain Res.* **1251**, 16–29 (2009).
55. D. A. Thayer, S. B. Yang, Y. N. Jan, L. Y. Jan, N-linked glycosylation of  $K_v1.2$  voltage-gated potassium channel facilitates cell surface expression and enhances the stability of internalized channels. *J. Physiol.* **594**, 6701–6713 (2016).
56. F. H. Yu, W. A. Catterall, The VGL-channome: A protein superfamily specialized for electrical signaling and ionic homeostasis. *Sci. STKE* **2004**, re15 (2004).
57. C. Sekirnjak *et al.*, Subcellular localization of the  $K^+$  channel subunit  $K_v3.1b$  in selected rat CNS neurons. *Brain Res.* **766**, 173–187 (1997).
58. A. Erisir, D. Lau, B. Rudy, C. S. Leonard, Function of specific  $K(+)$  channels in sustained high-frequency firing of fast-spiking neocortical interneurons. *J. Neurophysiol.* **82**, 2476–2489 (1999).
59. B. Tasic *et al.*, Adult mouse cortical cell taxonomy revealed by single cell transcriptomics. *Nat. Neurosci.* **19**, 335–346 (2016).
60. M. J. Rowan, E. Tranquil, J. M. Christie, Distinct Kv channel subtypes contribute to differences in spike signaling properties in the axon initial segment and presynaptic boutons of cerebellar interneurons. *J. Neurosci.* **34**, 6611–6623 (2014).
61. A. J. Labro, M. F. Priest, J. J. Lacroix, D. J. Snyders, F. Bezanilla,  $K_v3.1$  uses a timely resurgent  $K(+)$  current to secure action potential repolarization. *Nat. Commun.* **6**, 10173 (2015).
62. D. A. McCormick, D. Contreras, On the cellular and network bases of epileptic seizures. *Annu. Rev. Physiol.* **63**, 815–846 (2001).
63. K. Nakahira, G. Shi, K. J. Rhodes, J. S. Trimmer, Selective interaction of voltage-gated  $K(+)$  channel beta-subunits with alpha-subunits. *J. Biol. Chem.* **271**, 7084–7089 (1996).
64. A. Pantazis, R. Olcese, “Cut-open oocyte voltage-clamp technique” in *Encyclopedia of Biophysics*, G. Roberts, A. Watts, European Biophysical Societies, Eds. (Springer, Berlin, Heidelberg, 2019), pp. 1–9.
65. C. S. Gandhi, R. Olcese, The voltage-clamp fluorimetry technique. *Methods Mol. Biol.* **491**, 213–231 (2008).





**Supplementary Information for**

**An epilepsy-associated Kv1.2 charge-transfer-center mutation suppresses Kv1.2 and Kv1.4 subunit trafficking**

Michelle Nilsson, Sarah H. Lindström, Maki Kaneko, Kaiqian Wang, Teresa Mínguez-Viñas, Marina Angelini, Federica Steccanella, Deborah Holder, Michela Ottolia, Riccardo Olcese, Antonios Pantazis

Corresponding author: Antonios Pantazis  
Email: [antonios.pantazis@liu.se](mailto:antonios.pantazis@liu.se)

**This PDF file includes:**

Supplementary text  
Figures S1 to S6  
Table S1  
SI References

## Supplementary Information Text

### Tetramerization Model of specific stoichiometric trafficking: Alternatives and Assumptions

In this study, we propose that 3<sup>WT</sup>:1<sup>F233S</sup> K<sub>v</sub>1.2 hetero-tetramers are trafficking-capable, whereas all other stoichiometries are not. We also propose that only 3:1 and 2:2 K<sub>v</sub>1.4:K<sub>v</sub>1.2(F233S) hetero-tetramers can traffic. These findings primarily arise from the combination of “applied transcriptomics” electrophysiology (stringently controlling the RNA level of specific subunits over a broad range, at the single-cell level) with a model of binomial subunit tetramerization (Figs.5A & 7A); but they are also supported by results from additional experiments: concatemer electrophysiology, flow cytometry / immunocytochemistry and voltage-clamp fluorometry.

First, one might ask: “why hypothesize that specific stoichiometries are differentially trafficking-capable?” An alternative possibility is that all F233S-containing stoichiometries are able to traffic equally, but are less capable to do so than wild-type K<sub>v</sub>1.2 or K<sub>v</sub>1.4 homo-tetramers. In the case of K<sub>v</sub>1.2, while we cannot directly observe 3<sup>WT</sup>:1<sup>F233S</sup> heteromers, their preferential trafficking over 2<sup>WT</sup>:2<sup>F233S</sup> channels is supported by (i) the very poor trafficking of K<sub>v</sub>1.2(WT-F233S) concatemers, which emulate the 2:2 stoichiometry (Fig.5B,C) and (ii) the clear fluorescence signals from rescued F233S subunits in flow cytometry and VCF experiments (Figs. 4, S1, 8B). If all heteromers trafficked with 5% efficiency, it would be very difficult to detect them by optical methods. We simulated this condition with the binomial subunit tetramerization model by allowing all heteromers to traffic equally with specified efficiencies (Fig.S5): none of these models described the data as well. In the case of K<sub>v</sub>1.4, the answer is more clear: the K<sub>v</sub>1.4-K<sub>v</sub>1.2(F233S) concatemer, which emulates the 2:2 stoichiometry, trafficked with 100% efficiency (Fig.7D,E). If all stoichiometries of K<sub>v</sub>1.4/K<sub>v</sub>1.2(F233S) could traffic equally efficiently, then we would expect the purple curve to account for the data in Fig.7A. Ultimately, we cannot exclude some degree of trafficking of “non-permissible” stoichiometries; in fact, K<sub>v</sub>1.2(WT-F233S) concatemers do traffic with very low efficiency (5-6%). Our view is that the efficiency of heteromeric trafficking is *primarily* determined by the stoichiometric composition.

We must also consider two assumptions of the binomial subunit tetramerization models: (a) the total macroscopic conductance ( $G_{total}$ ) reflects the number of channels per condition, (b) K<sub>v</sub>1.2(F233S) subunits assemble in an unbiased manner with wild-type K<sub>v</sub>1.2 and K<sub>v</sub>1.4.

*a) The total macroscopic conductance ( $G_{total}$ ) reflects the number of channels per condition.*

The model outputs the frequency of specific tetrameric stoichiometries; these are compared to macroscopic conductance data, which are assumed to reflect the number of channels in the membrane. While the number of channels does contribute to the macroscopic conductance, two additional factors are maximal open probability (max  $P_o$ ) and single-channel conductance ( $\gamma$ ). If max  $P_o$  and  $\gamma$  were the same in all stoichiometries, then  $G_{total}$  alone would be an accurate measure of number of channels for all tested conditions.

If K<sub>v</sub>1.2(F233S) subunit inclusion decreased max  $P_o$  and  $\gamma$ , instead of channel trafficking, then one would expect no K<sub>v</sub>1.2(WT) or K<sub>v</sub>1.4 subunit sequestration; however, the latter is clearly evidenced in immunocytochemical experiments (Figs. 4, 6, S1).

If K<sub>v</sub>1.2 co-assembly with K<sub>v</sub>1.4 resulted in heteromers with higher max  $P_o$  or  $\gamma$  than K<sub>v</sub>1.4 homomers, it might be possible that the data in Fig.7A could be accounted for by only 3:1 K<sub>v</sub>1.4:K<sub>v</sub>1.2(F233S) hetero-tetramers, excluding the 2:2 stoichiometry. This possibility is unlikely since the K<sub>v</sub>1.4-K<sub>v</sub>1.2(F233S) concatemer supports 2:2 subunit trafficking (Fig.7D,E).

Ultimately, we cannot altogether exclude that some combination of max  $P_o$ ,  $\gamma$  and trafficking effects gave rise to the experimental data. The occurrence of such combinations is less parsimonious than simple trafficking defects; and the model findings in general are very well supported by experimental results.

*b) K<sub>v</sub>1.2(F233S) subunits assemble in an unbiased manner with wild-type K<sub>v</sub>1.2 and K<sub>v</sub>1.4.*

The binomial distribution of heteromers arises from the unbiased association of wild-type and mutant subunits. This is a reasonable assumption as (i) all K<sub>v</sub>1.2 and K<sub>v</sub>1.4 subunits have an intact N-terminal tetramerization domain that facilitates association even as the nascent peptide is

assembled by the ribosome (1); (ii) the mixed-subunit RNA is introduced to the oocyte at precisely the same place and time.

We can challenge this idea by introducing a negative association bias; *i.e.*, wild-type Kv1.2 subunits are less likely to co-assemble with Kv1.2(F233S). Effectively, this means that the availability of F233S subunits is diminished, which can be calculated by reducing the molar proportion of F233S by a factor  $<1$ . Conversely, multiplying by a factor  $>1$  increases its effective concentration. We explore both ideas in Fig.S6. Decreasing F233S effective concentration narrows the spread of the curves, such that Kv1.2 data are now better described by the black model (no heteromers / F233S-subunit rescue; Fig.S6B); and the Kv1.4 data by the green model (no 2:2 stoichiometry; Fig.S6E). However, both models are contradicted by experimental results from flow cytometry, VCF and concatemer experiments. Increasing F233S effective concentration splay out the curves. For Kv1.2, this means that data are best described by the cyan model (2:2 stoichiometry allowed; Fig.S6C); however this is inconsistent with concatemer experiments. No condition with bias  $>1$  could explain the Kv1.4 data better than unbiased association (Fig.S6F). To summarize, the “applied transcriptomics data”, in combination with other experiments in this work, favor unbiased heteromeric channel assembly.

As discussed, the data go a long way in rejecting most alternatives to specific stoichiometry trafficking. We cannot completely exclude contributions from other mechanisms (such as non-stringent stoichiometric trafficking, open probability / single-channel conductance, biased subunit association), nor is this necessary: the main conclusions of the model are both falsifiable and well supported by our experimental data, all the more impressive as the model carries no free parameters: model predictions are simply overlaid, not fit to the data.

## Materials & Methods

### Patient genetic testing

A HIPAA-compliant consent form by Children’s Hospital Los Angeles was signed by the patient’s parents. DNA was extracted from the peripheral blood of the patient and each of his unaffected parents as comparators using a commercially available kit (Promega Maxwell RSC DNA Extraction Kit). The exome sequencing library was generated for proband DNA using the Agilent SureSelect Human All Exon V6+Mito kit. Captured DNA fragments were then sequenced using the Illumina Nextseq 500 sequencing system, with  $2\times 100$  basepair (bp) paired-end reads. Single nucleotide variants (SNVs) and small insertions and deletions ( $<10$  bp) were detected by mapping and comparing the DNA sequences with the human reference genome (GRCh37-hg19). Of all the variants identified by exome sequencing, a list of rare variants (minor allele frequency  $<1\%$ ) located within a predefined set of 224 epilepsy associated genes (Table S1) was generated. These variants were further annotated and analyzed using Alissa Interpret (Agilent). The genes included in this panel are known to be associated with primary epilepsy, or associated with syndromes in which epilepsy is a commonly observed feature. The genes (Table S1) were evaluated for single nucleotide substitutions and small indels. Both parents and the patient were tested for the variant by Sanger sequencing (Fig.1D). Variant interpretation was done according to the standards and guidelines of variant interpretation by American College of Medical Genetics and Genomics and Association for Molecular Pathology (2).

### Molecular biology

Site-directed mutagenesis (SDM) to introduce F233S, A291C, *etc.*, was performed with a high-fidelity *Pfu* polymerase (Agilent 600850), unless otherwise stated. All molecular biology reagents were provided from New England Biolabs, and all synthetic oligonucleotides from Integrated DNA Technologies, unless stated otherwise. All molecular biology operations were confirmed by sequencing.



### *Immunocytochemistry constructs*

For initial two-color immunocytochemistry studies (Fig.2B-D), a plasmid containing rat Kv1.2 with an N-terminally fused EGFP tag (in the pEGFP-C1 vector) and an extracellular HA site (between transmembrane helices S1 and S2) was used; it was a generous gift from Lily Y. Jan (3, 4).

To incorporate a bungarotoxin binding site (BBS; TGG CGG TAC TAC GAG AGC AGC CTG GAG CCC TAC CCC GAC) in Kv1.2(HA) and Kv1.2(HA,F233S) constructs, the HA tag was excised using *BstEII* and *EcoRI* and replaced by a synthetic BBS-containing oligo. The resulting constructs had a BBS at the same position as the excised HA tag.

Rat brain Kv1.4 in the GW1 plasmid was gifted by James S. Trimmer (5). A hemagglutinin (HA) tag (TAT CCG TAC GAC GTC CCA GAC TAT GCG) was introduced at the S1-S2 extracellular linker after position G346. This was performed by excising a portion of the Kv1.4 N-terminus between unique sites *NotI* and *BsmI*, and replacing it with a gBlocks synthetic fragment including the HA tag sequence. The new construct was evaluated by cut-open oocyte Vaseline gap electrophysiology (see below): it exhibited fast N-type inactivation, and activated with a voltage-dependence similar to the tag-less channel  $\Delta V_{0.5} = -13 \pm 4 \text{ mV}$  ( $n=4$  per condition).

For four-color immunocytochemistry (Figs.4, 6, S1), HA-tagged channels were subcloned into pCDNA3-EGFP vectors (Addgene #13031, <http://n2t.net/addgene:13031> ; RRID:Addgene\_13031, a kind gift from Doug Golenbock) to make HA-tagged channels with an N-terminally-fused EGFP. Similarly, BBS-tagged channels were subcloned into pCDNA3-mRFP vectors (Addgene #13032, <http://n2t.net/addgene:13032> ; RRID:Addgene\_13032, a kind gift from Doug Golenbock).

### *Electrophysiology constructs*

The rat Kv1.2 cDNA construct in pMAX oocyte expression vector was a kind gift from Benoît Roux.

Rat Kv1.4 cDNA was subcloned from GW1 to pMAX. The inactivation-removed (IR,  $\Delta 2-61$ ) construct (6) was generated by excluding 177 bp immediately following the Kv1.4 ATG using the Q5 Site-Directed Mutagenesis kit.

To construct concatemeric dimers, a *BamHI* site was first introduced upstream of Kv1.4, to match the 5' untranslated region (UTR) of Kv1.2, by SDM. The existing Kv1.x ( $x=2, 2(\text{F233S})$  or 4) open reading frames (ORFs) would then become the C-terminal domains of the concatemer. N-terminal Kv1.x domains, originally generated by PCR amplification, were then introduced, along with a synthetic linker sequence modified from the 5' UTR of the *Xenopus*  $\beta$ -globin gene (7, 8). The N-terminal ORFs lacked a stop codon, and the sequence between the two Kv1.x domains was: GCT AGC GAT ACG AAG GAG CGA GGA AAC CTC TTC ACG TCA ACC GGA TCC GCC GCC ACC ATT (*NheI* and *BamHI* sites are underlined at the 5' and 3', respectively; bold indicates preserved pMAX sequence preceding the start codon of the C-terminal Kv1.x domain), which corresponds to the 20-residue linker: ASDTKERGNLFTSTGSAATI.

pMAX plasmids were linearized using *PacI*, transcribed to cRNA *in vitro* (T7 mMESSAGE MACHINE, Thermo Fisher Scientific) and stored at  $-80^\circ\text{C}$  in RNA storage solution (Thermo Fisher Scientific). cRNA was quantified spectrophotometrically and evaluated by gel electrophoresis.

### Immunocytochemistry & flow cytometry

**COS-7 cell culture and transfection:** COS-7 cells (ECACC 87021302) were grown in Complete Culture Medium containing: Dulbecco's modified Eagle's medium (DMEM)/F-12 Nutrient Mixture (1:1) (Gibco), heat-inactivated fetal bovine serum (FBS) (10%), penicillin (100 units), streptomycin (100 mg/ml) and glutamine (0.5 mM). Cultures were incubated at  $37^\circ\text{C}$  with 5%  $\text{CO}_2$  and passaged twice per week up to p-24. Cells used for flow-cytometry (FC) were seeded in 12-well plates (approx. 30,000 cells/well). Cells used for immunocytochemistry (ICC) were seeded in 35

mm glass-bottom dishes (approx. 15,000 cells/dish). Cells were transiently transfected 24 hr after seeding using TransIT-X2 Dynamic Delivery System (Mirus; pEGFP-C1 constructs, Fig.2B-D; ICC: 1.2µl TransIT-X2 : 0.6µg DNA; FC: 4µl TransIT-X2 : 1µg DNA) or jetOPTIMUS (Polyplus transfection; pCDNA3-EGFP/mRFP1 constructs, Figs.4, 6, S1; 1µl jetOPTIMUS : 1µg DNA).

*Immunocytochemistry / confocal microscopy:* Primary (Rat anti-HA; Roche 3F10) and secondary (AlexaFluor 568 conjugated goat anti-rat IgG(H+L); Invitrogen A-11077) antibodies were diluted 1:200 and 1:1000, respectively, in blocking solution. 48 hr post-transfection, COS-7 cells were rinsed with ice-chilled phosphate-buffered saline (PBS) supplemented with 0.9 mM Ca<sup>2+</sup> and 0.5 mM Mg<sup>2+</sup> (Gibco 14040-133). Cells were fixed with 4% paraformaldehyde in PBS (without Ca<sup>2+</sup> or Mg<sup>2+</sup>, 5 min), and washed with PBS (once quickly, then 3×5 min each) prior to incubation with blocking solution (2 ml of 5% normal goat serum in PBS) for at least 1 hr at room temperature. Blocking solution was replaced with primary antibody solution (0.5 ml) and cells were incubated at room temperature for at least 2 hrs. Cells were washed with PBS prior to incubation with secondary antibody solution (0.5 ml, 1 hr at room temperature). Unbound antibodies were washed off with PBS and a coverslip was mounted over the glass-bottom of each dish using ProLong Glass Antifade Mountant (Invitrogen P36982). Mountant was allowed to set for 18-24 hr at room temperature, then samples stored at 4°C. Confocal images were acquired using a Zeiss LSM 800 Microscope with Zen 2.3 software. A z-stack was acquired for each cell (z-section interval = 0.27 µm). Zen Analysis software was used to create an orthogonal projection of 2 sequential z-sections. Final images were prepared for publication using Adobe Photoshop CS6. Identical adjustments to levels, sharpness and pixel sampling were performed on all samples.

*Flow cytometry:* To quantify Kv1.2 subunit cell-surface expression (Fig.2D), COS-7 cells were harvested by trypsinization (0.05%) 48 hr post-transfection. Cells were washed with Dulbecco's PBS (DPBS, Gibco) and pelleted at 400 g for 5 min at 4°C. Cells were stained with Zombie Violet viability dye (BioLegend) and anti-HA conjugated Alexa Fluor 647 (Alexa Fluor 647 anti-HA.11 Epitope Tag Antibody; BioLegend Cat# 682404, RRID:AB\_2566616) as previously described (4, 9). Cells were detected using a Gallios Flow Cytometer (Beckman Coulter Life Sciences) as previously described (4). The fraction of anti-HA positive cells in the EGFP positive population, normalized to wild type Kv1.2(HA) measurements was calculated.

To evaluate Kv1.2(F233S) subunit surface trafficking in the presence or absence of Kv1.2(WT) or Kv1.4 subunits and *vice versa* (Figs.4, 6, S1), cells were stained with 8 µg/ml anti-HA conjugated Brilliant Violet 421 (Brilliant Violet 421 anti-HA.11 Epitope Tag Antibody; BioLegend Cat# 682405, RRID: AB\_2716037) and 1 µg/ml α-bungarotoxin-conjugated Alexa Fluor 647 (Invitrogen, #B35450) in 100 µl DPBS/5% FBS for 45 min at 4°C. Cells were washed with (i) DPBS/5% FBS and (ii) DPBS. Finally, a single-cell suspension was prepared using pre-separation filters (Miltenyi Biotec) (70µm) and stored at 4°C in the dark until detection later the same day (4, 9). Cells were detected using a BD FACSAria III Cell Sorter. Brilliant Violet 421, EGFP, mRFP1 and BTX 647 were excited at 405, 488, 561 and 633 nm respectively. Detection was filtered for wavelengths 450/40, 550/30, 610/20 and 660/20 nm. Cell clumps or fragments were excluded using forward and side scatter gating. Positive gates for Brilliant Violet 421, EGFP, mRFP1 and BTX 647 were set using untransfected cells, negative controls for anti-HA or BTX and fluorescence-minus-one controls. Spillover between channels were compensated in single color controls: EGFP-Kv1.2(WT) or mRFP1-Kv1.2(WT). Only EGFP and mRFP1 double-positive cells per replicate were counted. Data were analyzed using Kaluza Analysis 1.3 (Beckman Coulter Life Sciences) and Microsoft Excel.

#### Electrophysiology & voltage-clamp fluorometry

*Oocyte preparation:* All animal experiments were approved by the Linköping University Animal Care and Use Committee. Defolliculated *Xenopus laevis* oocytes were either purchased from Ecocyte or isolated and prepared from locally-kept *Xenopus laevis* (Nasco, WI, USA) as follows: Frogs were anesthetized with 1.4g/L tricaine (ethyl 3-aminobenzoate methanesulfonate, Sigma #A5040). Lobes of ovaries were removed through an abdominal incision and placed into Ca<sup>2+</sup>-free OR-2 solution (in mM: 82.5 NaCl, 2.5 KCl, 1 MgCl<sub>2</sub> and 5 HEPES; pH adjusted to 7.4 by

NaOH) for further processing. Frogs were treated with analgesics (5mg/mL Marcain; Astra Zeneca & 2% Xylocain gel; Aspen) and the incision was sutured, prior to being returned to a recovery aquarium for post-surgical monitoring. Ovaries were cut into small clusters of 5-7 oocytes, then enzymatically treated with Liberase TM (7 Units/batch; Roche 05401127001) in ~10 ml of OR-2 with agitation using an orbital shaker for 25-40 min. Liberase was removed by washing with OR-2 solution, then manual agitation for 30-60 min was employed to remove follicular layers. Mature (stage V-VI) defolliculated oocytes were selected and stored at 17°C in SOS (in mM: 100 NaCl, 2 KCl, 1.8 CaCl<sub>2</sub>, 1 MgCl<sub>2</sub> and 5 HEPES; pH adjusted to 7.0 by NaOH).

*Parallel two-electrode voltage clamp (TEVC) recordings:* Oocytes were injected with 50 nl of cRNA solution using a nanoinjector (UMP3T-1, World Precision Instruments). Specific cRNA amounts used are mentioned in their corresponding experiments. One day after injection, oocytes were recorded using a medium throughput robot capable of eight simultaneous TEVC recordings (OpusXpress 6000A Parallel Oocyte Voltage Clamp; Axon Instruments). Recording electrodes were pulled from TW150F-6 thin-wall capillary glass (World Precision Instruments) on a P-1000 horizontal puller (Sutter Instruments). Only electrodes with resistance  $\leq 1 \Omega$  (I-electrodes), or  $\leq 1.5 \Omega$  (V-electrodes) were used. Electrodes were filled with 3 M KCl. The oocyte recording chambers were perfused continuously with SOS. Once oocytes in all chambers were correctly impaled by both electrodes, oocytes were clamped at a holding potential of  $-80\text{mV}$ . P/-6 subtraction was used to limit capacitive transients. For Kv1.2(WT/F233S) experiments (Figs. 3, 5A, S2A,B), voltage-dependent activation was evaluated using a series of 100ms test-pulses from  $-80\text{mV}$  to  $120\text{mV}$  in 10-mV increments. For experiments including Kv1.4 subunits (Figs. 7A-C, S3), voltage-dependent activation was evaluated using a series of 100ms test-pulses (from  $-90\text{mV}$  to  $100\text{mV}$  in 10-mV increments). A pre-pulse to  $-120\text{mV}$  for 800ms preceded each test-pulse to completely relieve N-type inactivation. A 10 s inter-pulse interval was used in all recordings. Current was low-pass filtered to 2 kHz and acquired at 6.25 kHz using the OpusXpress digitizer and OpusXpress 1.1 software (Axon Instruments).

*Cut-open oocyte Vaseline gap (COVG) recordings:* COVG is a low-noise, fast voltage clamp technique (10-12). A Clampator One CA-1 amplifier (Dagan) was used in COVG mode. Its C95 capacitor was replaced by one of 470 pF to improve capacitive transient compensation. The oocyte was placed in a triple-compartment Perspex chamber, with a diameter of 600  $\mu\text{m}$  for the top and bottom apertures. The upper chamber isolated the oocyte's upper domus and maintained it under clamp. The middle chamber provided a guard shield by clamping the middle part of the oocyte to the same potential as the upper chamber. The bottom chamber injected current intracellularly, through the saponin-permeabilized part of the oocyte. External solution (mM): 120 Na-methanesulfonate (MeS), 2 K-MeS, 2 Ca(MeS)<sub>2</sub>, 10 HEPES (pH=7.0). Internal solution (mM): 120 K-glutamate, 10 HEPES (pH=7.0). Intracellular micro-pipette solution (mM): 2700 Na-MeS, 10 NaCl. Low access resistance to the oocyte interior was obtained by permeabilizing the oocyte with 0.1% saponin carried by the internal solution. In VCF experiments (set-up and staining procedures described below), holding potential was  $-80\text{mV}$ . All pulses were preceded by a 800ms pre-pulse to  $-120\text{mV}$ . 100-ms pulses were used ( $-120\ldots 160\text{mV}$ ,  $\Delta V=20\text{mV}$ ) with inter-pulse duration of 10 s. Current was filtered to 5 kHz using the Dagan on-board low-pass Bessel filter. Data were acquired at 25 kHz using a Digidata 1550B1 digitizer and pClamp v.11 software (Molecular Devices).

*Voltage clamp fluorometry (VCF):* VCF was performed by adding epifluorescence and light detection capability to the COVG system (12, 13). Prior to mounting on the COVG apparatus, oocytes were stained at room temperature for 5 minutes with 20  $\mu\text{M}$  MTS-TAMRA fluorophore in a depolarizing solution (in mM: 120 K-MeS, 2 Ca(MeS)<sub>2</sub>, 10 HEPES, pH=7.0), in the dark, to label the introduced Cys (A291C). The oocytes were then rinsed in dye-free SOS prior to being mounted in the recording chamber. Fluorescence emission and ionic current were simultaneously measured from the same area of membrane isolated by the top chamber. The same electrophysiological apparatus and solutions were used as above. The optical setup consisted of an Olympus BX51WI upright microscope with filters (Semrock Brightline) appropriate for rhodamine excitation and emission wavelengths (exciter: FF01-531/40-25; dichroic: FF562-Di02-25x36; emitter: FF01-593/40-25). The light source was a 530 nm, 170 mW LED (M530L3-C1,



Thorlabs) driven by a Cyclops LED driver (Open Ephys). The objective (Olympus LUMPLANFL, 40XW, water immersion) had a numerical aperture of 0.8 and a working distance of 3.3 mm, which left sufficient room for the insertion of the microelectrode while fully covering the oocyte domus exposed in the external recording chamber. The emission light from the camera port was focused on a Si photodiode (SM05PD3A, Thorlabs) connected to a current amplifier (DLPCA-200, FEMTO). Its output was filtered to 5 kHz using an in-line low-pass Bessel filter (LPF-8, Warner Instruments) before being acquired at 25 kHz (Digidata 1550B1 and pClamp v.11, Molecular Devices).

### Data analysis and modeling

*Electrophysiological data analysis:* All electrophysiological data analysis was performed by least squares fitting in Microsoft Excel. In experiments with just Kv1.2 subunits, steady-state activation was calculated by fitting the macroscopic conductance to a Boltzmann distribution:

$$G = \frac{G_{\text{total}}}{1 + \exp\left[\frac{zF}{RT}(V_{0.5} - V_m)\right]} \quad [1]$$

where  $V_m$  was the membrane potential;  $V_{0.5}$  was the half-activation potential;  $z$  was the effective valence;  $F$  and  $R$  the Faraday and Gas constants, respectively;  $T$  was temperature (294 K). The maximal macroscopic conductance,  $G$ , was calculated by dividing the current ( $I_m$ ) by the driving force:

$$G = \frac{I_m}{V_m - E_K} \quad [2]$$

where  $E_K$  was the equilibrium potential for potassium. In TEVC experiments, the  $V_m$  reported by OpusXpress at the same time as the sampled  $I_m$  was used.

In experiments with Kv1.4 subunits, peak current was used. The G-V curve could be better accounted-for with the sum of two Boltzmann distributions:

$$G = G_{\text{total}} \sum_{i=1}^2 \frac{w_i}{1 + \exp\left[\frac{z_i F}{RT}(V_{0.5,i} - V_m)\right]} \quad [3]$$

where  $w$  is the fractional contribution, or weight, of each component, and  $w_1 = 1 - w_2$ .

The voltage dependence of fluorescence deflections ( $\Delta F$ ; *i.e.*, VSD activation) was estimated by fitting  $\Delta F$  to a Boltzmann distribution:

$$\Delta F = \frac{\Delta F_{\text{max}} - \Delta F_{\text{min}}}{1 + \exp\left[\frac{zF}{RT}(V_{0.5} - V_m)\right]} + \Delta F_{\text{min}} \quad [4]$$

where  $\Delta F_{\text{max}}$  and  $\Delta F_{\text{min}}$  were the maximal and minimal  $\Delta F$  asymptotes, respectively.

*Binomial models of heteromeric channel configurations:* The probability that a tetrameric channel with specific subunit composition will form was calculated starting with the standard binomial distribution:

$$f(n, k, p) = \binom{n}{k} p^k (1-p)^{n-k} \quad [5]$$

where  $n$  is the number of trials (always 4, for the obligate tetrameric  $K_v$  channels);  $k$  is the number of “successes”, *i.e.*,  $K_v1.2(WT)$  or  $K_v1.4$  subunits in the tetramer ( $k=4$  for WT homo-tetramers,  $k=3$  for 3:1 WT:F233S hetero-tetramers, and so on);  $p$  is the probability to encounter a  $K_v1.2(WT)$  or  $K_v1.4$  subunit during tetramerization, given by:

$$p = \frac{1}{m+1} \quad [6]$$

where  $m$  is the relative molar proportion of injected  $K_v1.2(F233S)$  cRNA, ranging from 0 to 8.

In these experiments (Figs. 5A, 7A), the molar proportion of  $K_v1.2(F233S)$  cRNA increased, while the amount of  $K_v1.2(WT)$  or  $K_v1.4$  cRNA was kept stable. Therefore, more tetramers could potentially be made with higher F233S proportions due to the increased availability of  $K_v$  subunits. For this reason, the frequency of tetramers ( $f$ , eq.[5]) was scaled by the relative amount of cRNA:

$$g = f(n, k, p) \cdot (m+1) \quad [7]$$

The black curves in the model (Figs. 5A, 7A) represent  $g$  with  $k=4$ ; the green curves are the sum of  $g$  with  $k=4$  and  $k=3$ ; and so on.

**Statistics:** All comparative statistics (*e.g.*, “relative  $G_{total}$ ” or “ $\Delta V_{0.5}$ ”) were performed among oocytes or COS-7 cells from the same block of experiments (same batch / passage number, RNA injection / DNA transfection, and experiment day). All significance tests were two-tailed Student’s  $t$ -tests. Errors are SEM or 95% confidence intervals (C.I.), as stated in the figure legends.

## Supplementary Figures

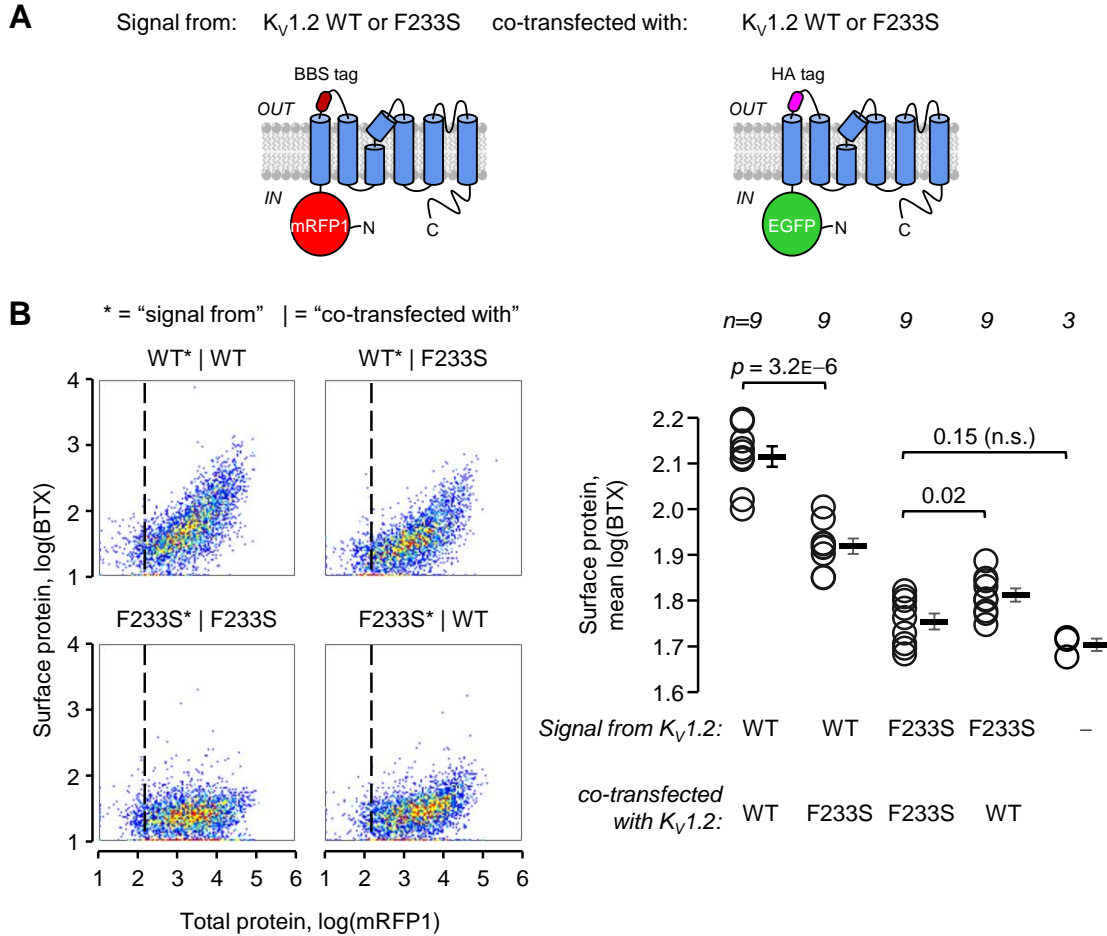


**Fig. S1:  $K_v1.2$ (F233S) subunits sequester, and are concomitantly rescued by,  $K_v1.2$ (WT): the “flipped construct” experiment.** Same dataset as in the experiment in Fig.4, showing the surface signals from BBS constructs. **(A)** Constructs used to evaluate  $K_v1.2$  cell surface trafficking. Each construct represents one allele. (i)  $K_v1.2$  with N-terminally fused mRFP1, reporting total protein production; and an extracellular bungarotoxin binding-site (BBS) tag, co-transfected with (ii)  $K_v1.2$  with N-terminally fused EGFP, reporting total protein production; and an extracellular hemagglutinin (HA) tag. **(B)** Representative cell density plots of log(mRFP1) (total protein) against log(BTX) (cell surface expression) from cells positive for EGFP signal. WT\*: mRFP1- $K_v1.2$ (BBS); WT: EGFP- $K_v1.2$ (HA); F233S\*: mRFP1- $K_v1.2$ (BBS,F233S); F233S: EGFP- $K_v1.2$ (HA,F233S). The vertical dashed line separates negative (left) and positive (right) mRFP1 cells among the plotted live, EGFP-positive cells. Percentage of cells with positive surface (BTX) signal (normalized to WT\*|WT, i.e.,  $100 \pm 4.7\%$ ): WT\*|F233S:  $42 \pm 3.4\%$ ; F233S\*|WT:  $13 \pm 2.2\%$ ; F233S\*|F233S:  $5.5 \pm 1.1\%$ . Mean surface protein intensity (log(BTX)) from live, EGFP- and mRFP1-positive cells. Error bars are  $\pm$ SEM. n.s.= not significant.

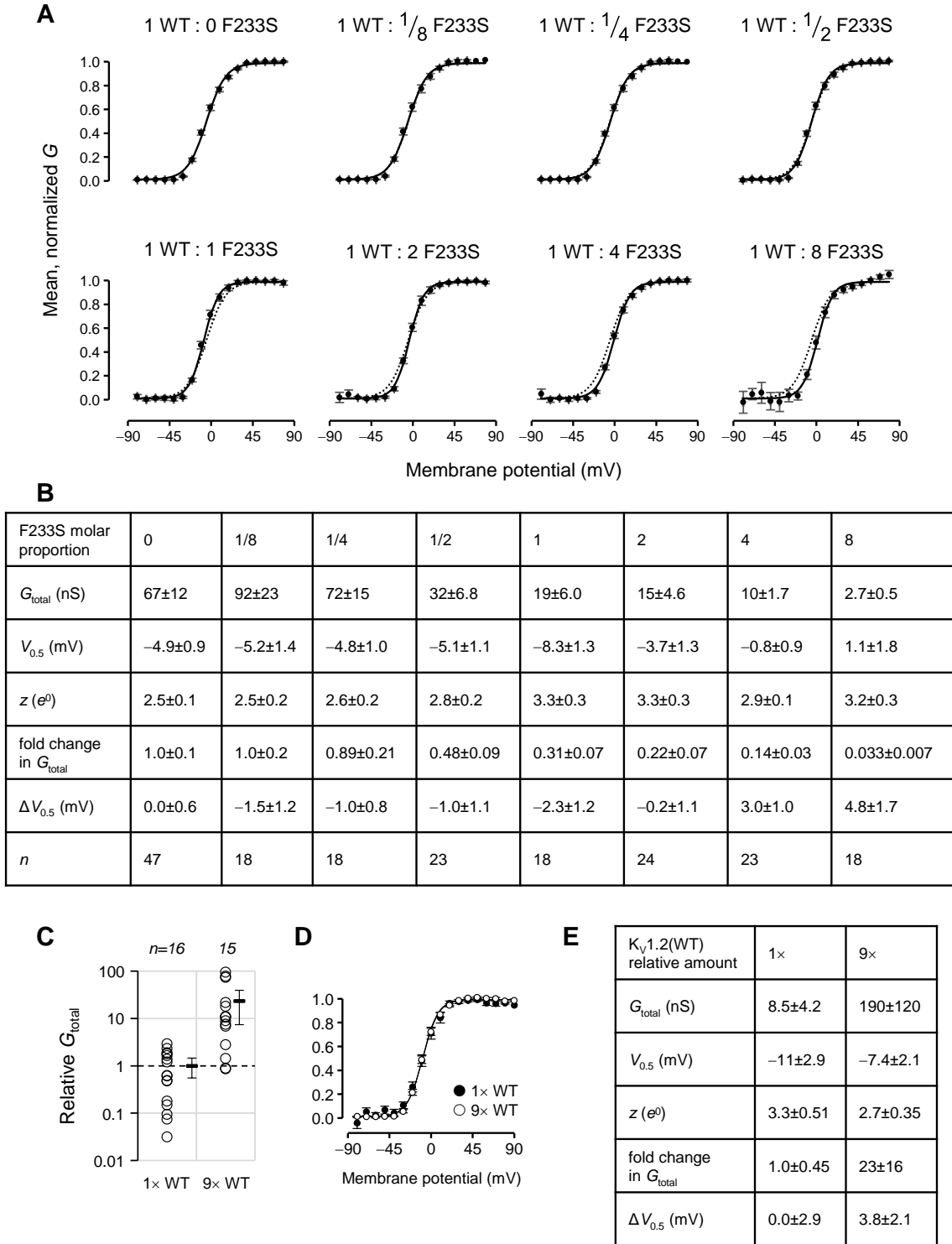
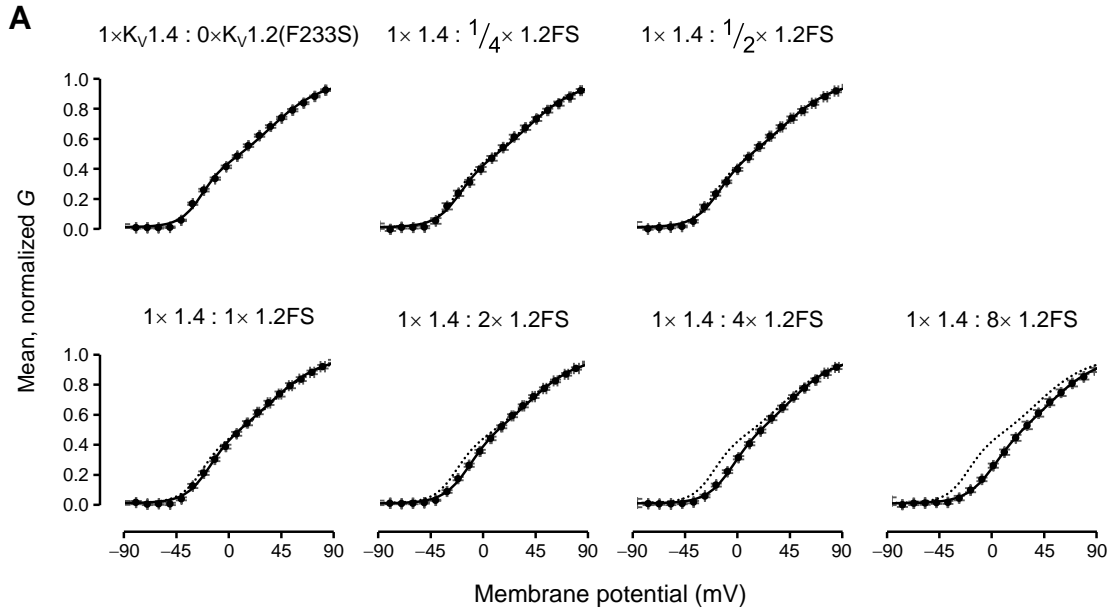


**Fig. S2: Currents from oocytes injected with  $K_v1.2(\text{WT})$  and increasing proportions of  $K_v1.2(\text{F233S})$  exhibit similar voltage dependence. (A)** Mean, normalized conductance (filled circles) and Boltzmann distribution fits (solid line) from the experiments in Fig.5A. The dotted line is the Boltzmann fit of 1 WT : 0 FS (top-left). **(B)** Boltzmann distribution parameters (see eq.1) for the fits in panel A. **(C)** Oocytes were injected with 9-fold  $K_v1.2(\text{WT})$  cRNA, to evaluate oocyte capacity to process this amount of cRNA. Their macroscopic conductance was  $23\pm8.2$ -fold

relative to oocytes expressing 1× RNA (*i.e.*, 0.5ng/oocyte). This amount is not statistically significant from a sample with mean=9 (*i.e.*, 9-fold increase in conductance) and the same standard deviation and number of observations ( $p=0.21$ ). This experiment was performed under COVG, to handle the increased conductance, up to 730  $\mu$ S, with better voltage control; in addition, current is recorded from 20% of the oocyte surface area (12), further decreasing macroscopic currents that could generate clamp errors. It shows that the conductance observed in the presence of increasing F233S cRNA (Figs.5A & 7A) was not under-estimated due to potential oocyte translation issues. **(D)** Voltage dependence of 1× and 9× WT RNA condition. **(E)** Parameters for the analysis in panes C and D. Errors are 95% C.I..





**B**

F233S molar proportion	0	1/4	1/2	1	2	4	8
$G_{\text{total}}$ (nS)	28±4.0	26±6.4	39±11	39±9	49±8	28±4	15±3.4
$V_{0.5, 1}$ (mV)	-23±1.0	-20±2.5	-19±1.2	-16±1.3	-11±1.3	-6.9±1.1	-0.5±2.4
$z_1$ (e <sup>0</sup> )	2.8±0.1	2.7±0.2	2.4±0.1	2.5±0.2	2.3±0.1	2.3±0.1	2.2±0.2
$w_2$	0.65±0.01	0.63±0.02	0.61±0.02	0.59±0.01	0.58±0.01	0.60±0.01	0.60±0.05
$V_{0.5, 2}$ (mV)	38±1.5	41±3.0	40±2.0	41±2.7	45±1.8	46±2.0	52±4.5
$z_2$ (e <sup>0</sup> )	1.1±0.02	1.1±0.04	1.1±0.04	1.2±0.04	1.2±0.02	1.2±0.03	1.2±0.05
$V_{0.5}$ (mV)	12±1.4	14±2.4	11±1.7	12±2.2	15±1.6	20±1.4	27±2.7
$V_{0.2}$ (mV)	-25±0.8	-22±2.1	-22±1.1	-20±1.3	-16±1.2	-11±1.0	-5.5±1.5
fold change in $G_{\text{total}}$	1.0±0.10	0.78±0.13	1.4±0.32	1.5±0.26	1.44±0.30	0.83±0.12	0.48±0.11
$\Delta V_{0.5}$ (mV)	0.0±1.2	2.7±1.7	-0.4±1.9	-0.3±2.0	3.3±1.7	8.0±1.4	16±2.5
$\Delta V_{0.2}$ (mV)	0.0±0.6	2.2±1.7	2.8±0.9	4.4±1.1	9.0±1.2	14±0.8	19±1.1
$n$	43	18	22	30	23	23	18

**Fig. S3: Boltzmann parameters for K<sub>V</sub>1.4 channels coexpressed with increasing amount of K<sub>V</sub>1.2(F233S).** (A) Mean, normalized conductance (filled circles) and Boltzmann distribution fits (solid line) from the experiments in Fig.7A,B. The dotted line is the Boltzmann fit of 1× K<sub>V</sub>1.4 : 0× K<sub>V</sub>1.2(F233S) (top-left). (B) Boltzmann distribution parameters (see eq.3) for the curves in panel A and Fig.7B. Errors are ±95% C.I.

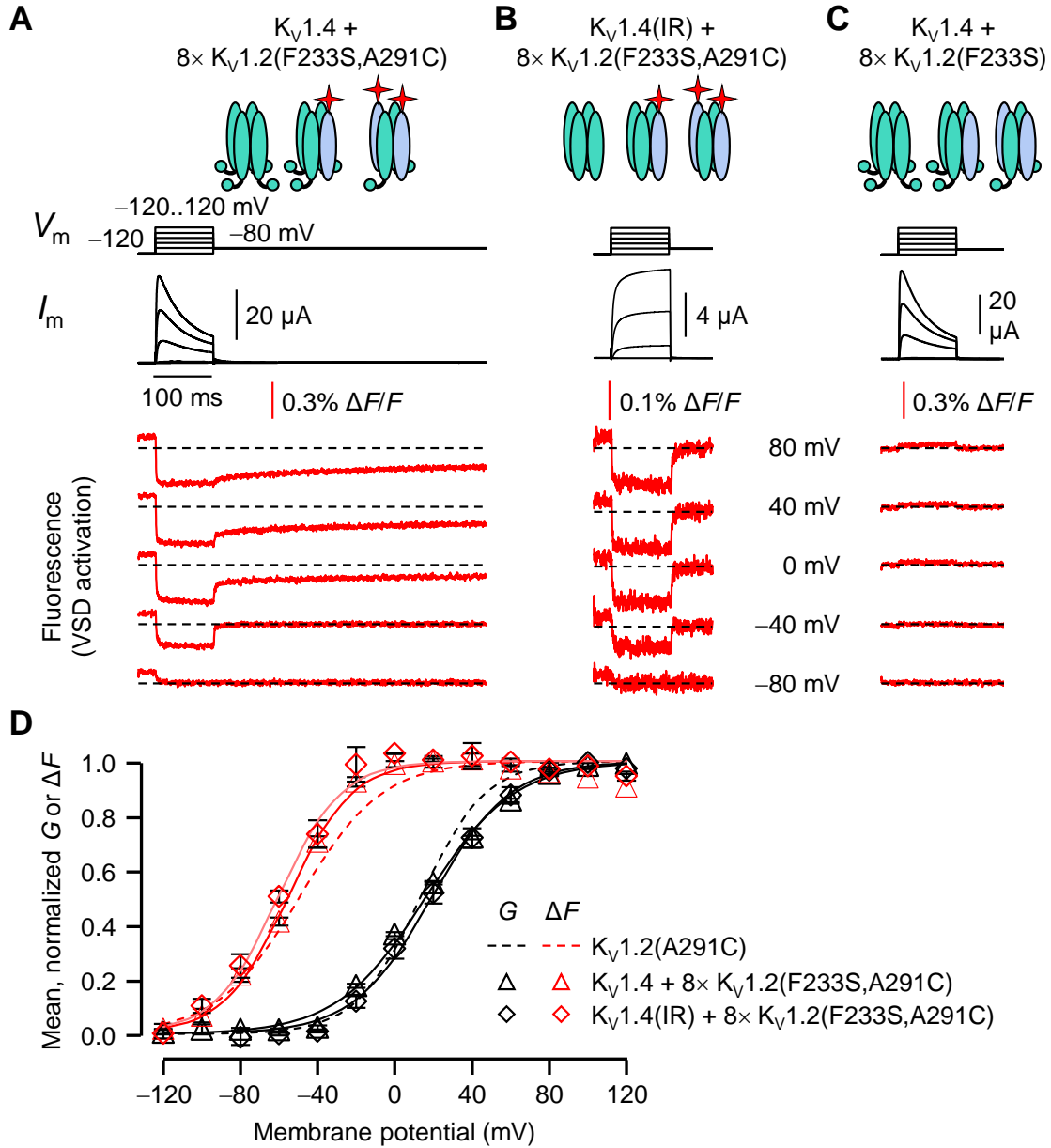


**Fig. S4: Voltage-clamp fluorometry controls.** **(A)** Voltage-clamp fluorometry (VCF) experiments on  $K_v1.2(F233S)$  subunits rescued by  $K_v1.4$ . Reproduced from Fig.8C, for reference. Note that VSD deactivation is very slow at potentials where channels open, and undergo N-terminal inactivation (charge immobilization). **(B)** VCF experiments on  $K_v1.2(F233S)$  subunits rescued by  $K_v1.4$  lacking their inactivation particle (inactivation-removed, IR). Note that the channels do not inactivate, and the VSDs deactivate rapidly. **(C)** As in A, without A291C (negative fluorescence control). **(D)** Normalized macroscopic conductance ( $G$ , black) and VSD activation ( $\Delta F$ , red), fit to Boltzmann distributions.  $K_v1.2(A291C)$   $G$ :  $V_{0.5}=14 \pm 2.8$  mV;  $z_{eff}=1.6 \pm 0.14$   $e^0$ ;  $\Delta F$ :  $V_{0.5}=-50 \pm 1.8$  mV;  $z_{eff}=1.3 \pm 0.22$   $e^0$ ;  $n=4$ .  $K_v1.2(F233S, A291C)/1.4$   $G$ :  $V_{0.5}=16 \pm 0.75$  mV;  $z_{eff}=1.1 \pm 0.039$   $e^0$ ;  $\Delta F$ :  $V_{0.5}=-56 \pm 1.0$  mV;  $z_{eff}=1.6 \pm 0.13$   $e^0$ ;  $n=6$ . Errors are SEM.  $K_v1.2(F233S, A291C)/1.4(IR)$   $G$ :  $V_{0.5}=18$  [15,23] mV;  $z_{eff}=1.3$  [1.3,1.2]  $e^0$ ;  $\Delta F$ :  $V_{0.5}=-61$  [-63, -58] mV;  $z_{eff}=1.6$  [1.4,1.7]  $e^0$ ;  $n=2$ . Error bars represent the two observations.

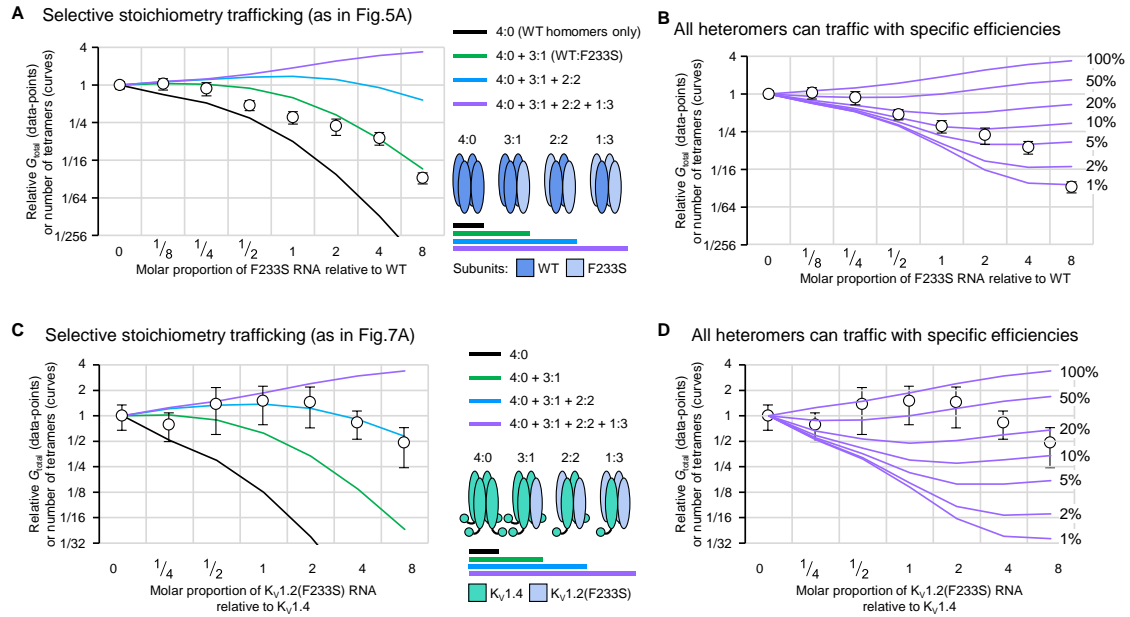


**Fig. S5: Models with selective stoichiometry trafficking fit data better than those with equal heteromer trafficking efficiency.** See Supplemental Discussion. **(A)** Reproduced from Fig.5A, the model shows that the trafficking of only 3WT:1F233S heterotetramers (as well as WT homo-tetramers) account for the data very well (green curve). **(B)** Same data as in A, but overlaid with models predicting equal trafficking efficiency for all hetero-tetramers, as specified. The curve with 100% efficiency is the same as the purple curve in A. The trafficking of WT homomers was always 100%. **(C,D)** as in A and B, for the  $K_v1.4$  experiment (Fig.7A). Note that none of the curves in B and D describe the data as well as curves in A and C. While some do approximate the data (2% in B, and 20% efficiency in D), they contradict other experimental findings. Specifically, very low heteromeric trafficking efficiency in B contradicts the strong fluorescence signals showing F233S subunit rescue in immunocytochemistry (Figs. 4, S1) and VCF (Fig.8B) experiments. The 20% efficiency in D contradicts the  $\approx 100\%$  trafficking efficiency of  $K_v1.4$ - $K_v1.2$ (F233S) concatemers in Fig.7D,E.

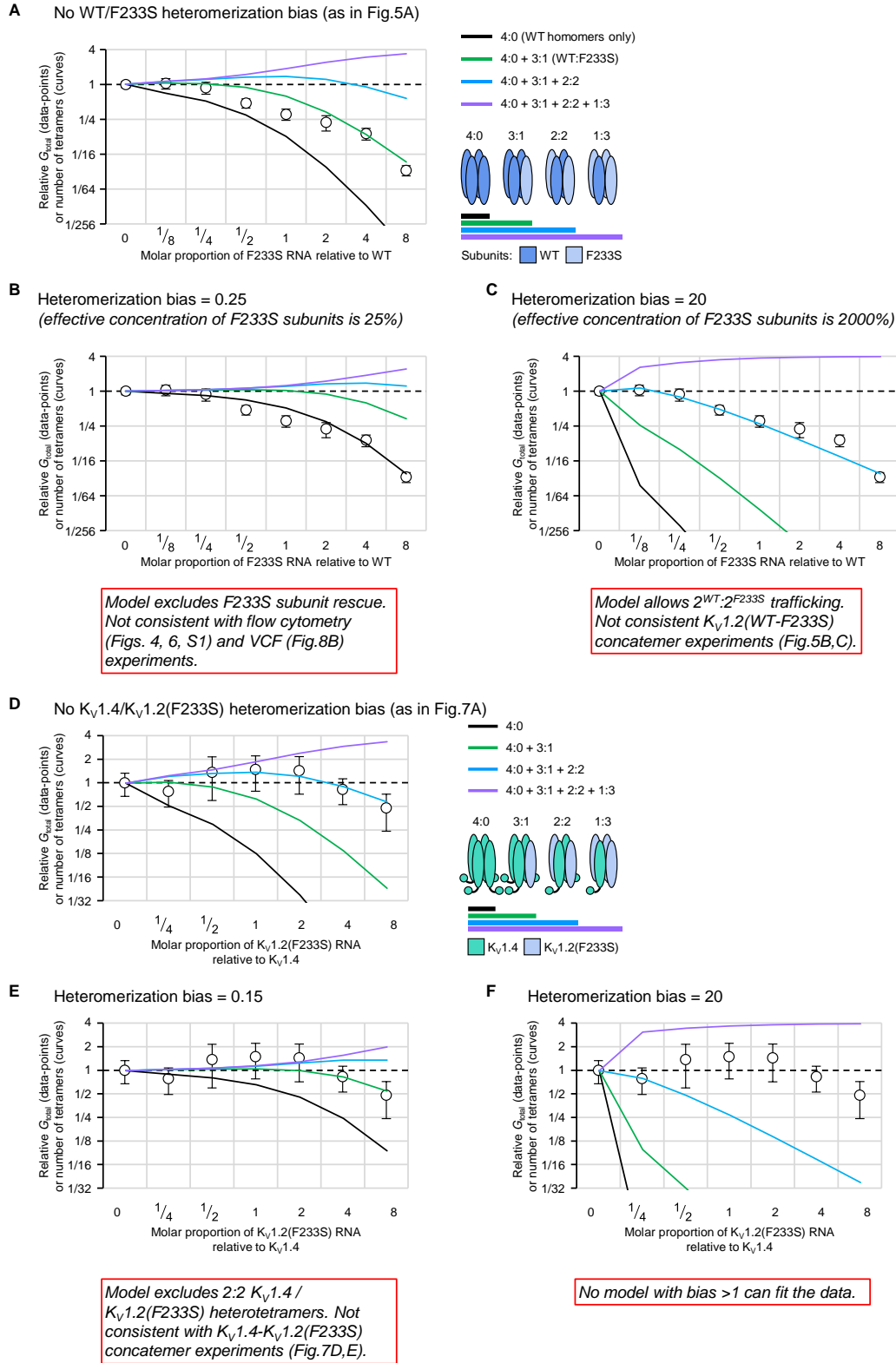


**Fig. S6: Bias for, or against, heteromeric assembly is not consistent with experimental data.** Tetramerization models incorporating negative (<1) or positive (>1) bias for heteromeric assembly between  $K_v1.2(F233S)$  and wild-type  $K_v1.2$  (A-C) or  $K_v1.4$  (D-F). See Supplemental Discussion.

**Table S1:** Screened genes, and percentage of their coding region covered at a minimum of 10 reads

Gene	%	Gene	%	Gene	%	Gene	%	Gene	%	Gene	%	Gene	%	Gene	%
ABAT	99.99	CARS2	96.88	DOCK7	99.99	GLRA1	100	KCTD7	100	PGAP2	100	SCARB2	100	STRADA	99.63
ADGRG1	100	CASK	99.96	DPAGT1	100	GLUD1	98.14	KPTN	100	PHGDH	100	SCN1A	100	STX1B	100
ADPRHL2	100	CASR	100	DYNC1H1	100	GNAO1	100	LGI1	99.98	PIGA	98.54	SCN1B	99.77	STXBP1	100
ADSL	100	CDKL5	99.87	DYRK1A	100	GNB1	100	LIAS	100	PIGG	99.21	SCN2A	99.91	SUOX	100
AFG3L2	99.05	CHD2	100	EARS2	100	GOSR2	99.98	MBD5	100	PIGN	99.76	SCN3A	100	SYN1	99.81
AKT3	99.98	CHRNA2	100	EEF1A2	100	GPHN	100	MBOAT7	100	PIGO	100	SCN8A	100	SYNGAP1	94.64
ALDH5A1	100	CHRNA4	99.88	EFHC1	100	GRIN1	100	MECP2	99.98	PIGT	100	SEPSECS	100	SYNJ1	99.98
ALDH7A1	99.11	CHRN2B	100	EHMT1	97.03	GRIN2A	100	MEF2C	99.63	PIGV	100	SERPINI1	100	SZT2	100
ALG11	100	CLCN4	99.88	EPM2A	92.06	GRIN2B	99.91	MFSD8	100	PLCB1	100	SHH	100	TBC1D24	100
ALG13	99.78	CLN3	100	EXOSC3	98.74	GRIN2D	99.1	MLC1	100	PLPBP	100	SIK1	100	TBCK	99.92
ALPL	100	CLN5	100	FARS2	100	HCN1	100	MOCS1	99.52	PNKP	99.99	SIX3	100	TCF4	100
AMT	100	CLN6	99.98	FGF12	100	HECW2	99.99	MOCS2	100	PNPO	100	SLC12A5	100	TPP1	100
AP3B2	99.67	CLN8	100	FLNA	100	HNRNPU	100	NARS2	94.12	POLG	100	SLC13A5	100	TRAK1	99.23
ARFGEF2	100	CLTC	100	FOLR1	100	HSD17B10	100	NDE1	100	PPP3CA	99.98	SLC19A3	99.97	TRIM8	100
ARHGEF9	98.69	CNKS2	99.9	FOXP1	97.47	IER3IP1	99.97	NECAP1	100	PPT1	100	SLC1A2	100	TRPM6	100
ARX	97.86	CNTNAP2	99.98	FRRS1L	94.03	IQSEC2	98.52	NEDD4L	99.99	PRICKLE1	100	SLC25A12	100	TSC1	99.99
ASAH1	99.97	COL4A1	99.96	GABBR2	99.89	IRF2BPL	99.97	NEXMIF	100	PRRT2	100	SLC25A22	100	TSC2	100
ASPM	99.89	COQ4	99.99	GABRA1	100	ITPA	97.33	NGLY1	100	PRUNE1	100	SLC2A1	100	TSEN2	98.67
ASXL3	99.93	CPLX1	100	GABRA2	99.99	KANSL1	99.95	NHLRC1	100	PSAT1	99.07	SLC35A2	98.86	TSEN54	96.82
ATP1A2	99.99	CSTB	100	GABRB2	100	KCNA2	100	NPRL3	100	PSPH	100	SLC35A3	99.97	TUBA1A	100
ATP1A3	100	CTSD	100	GABRB3	99.94	KCNB1	100	OPHN1	99.93	PTCH1	100	SLC6A1	100	TUBB2A	99.96
BCKDK	100	CUL4B	99.95	GABRG2	99.23	KCNC1	100	OTUD6B	100	PURA	100	SLC6A8	99.99	UBA5	100
BRAT1	99.99	DCX	100	GAMT	99.99	KCNJ10	100	PACS1	100	QARS	100	SLC9A6	99.96	UBE3A	99.55
C12orf57	100	DENND5A	100	GATM	100	KCNMA1	100	PACS2	100	RARS2	98.55	SMC1A	99.9	WDR45	99.08
CACNA1A	99.61	DEPDC5	99.62	GCSH	99.67	KCNQ2	100	PAFAH1B1	99.73	RELN	100	SNAP25	100	WDR62	100
CACNA1D	100	DIAPH1	98.42	GFAP	99.9	KCNQ3	100	PARS2	100	RFT1	99.99	SPATA5	100	WDR73	100
CACNA2D2	99.64	DNM1	100	GLDC	99.56	KCNT1	99.86	PCDH12	100	ROGDI	99.93	SPTAN1	100	WWOX	100
CAD	100	DNM1L	99.99	GLI2	100	KCNT2	99.98	PCDH19	99.97	RORA	99.76	ST3GAL5	99.66	ZEB2	100



## SI references

1. J. Lu, J. M. Robinson, D. Edwards, C. Deutsch, T1-T1 interactions occur in ER membranes while nascent Kv peptides are still attached to ribosomes. *Biochemistry* **40**, 10934-10946 (2001).
2. S. Richards *et al.*, Standards and guidelines for the interpretation of sequence variants: a joint consensus recommendation of the American College of Medical Genetics and Genomics and the Association for Molecular Pathology. *Genet Med* **17**, 405-424 (2015).
3. C. Gu, Y. N. Jan, L. Y. Jan, A conserved domain in axonal targeting of Kv1 (Shaker) voltage-gated potassium channels. *Science* **301**, 646-649 (2003).
4. A. Pantazis *et al.*, Tracking the motion of the KV 1.2 voltage sensor reveals the molecular perturbations caused by a de novo mutation in a case of epilepsy. *J Physiol* **598**, 5245-5269 (2020).
5. K. Nakahira, G. Shi, K. J. Rhodes, J. S. Trimmer, Selective interaction of voltage-gated K<sup>+</sup> channel beta-subunits with alpha-subunits. *J Biol Chem* **271**, 7084-7089 (1996).
6. S. Kondoh, K. Ishii, Y. Nakamura, N. Taira, A mammalian transient type K<sup>+</sup> channel, rat Kv1.4, has two potential domains that could produce rapid inactivation. *J Biol Chem* **272**, 19333-19338 (1997).
7. A. Ray (2017) Development of novel concatemer technology using potassium channel (Kv1.1) homotetramer as a framework.
8. S. Akhtar, O. Shamotienko, M. Papakosta, F. Ali, J. O. Dolly, Characteristics of brain Kv1 channels tailored to mimic native counterparts by tandem linkage of alpha subunits: implications for K<sup>+</sup> channelopathies. *J Biol Chem* **277**, 16376-16382 (2002).
9. B. Bourdin, E. Segura, M. P. Tetreault, S. Lesage, L. Parent, Determination of the Relative Cell Surface and Total Expression of Recombinant Ion Channels Using Flow Cytometry. *J Vis Exp* 10.3791/54732 (2016).
10. M. Taglialatela, L. Toro, E. Stefani, Novel voltage clamp to record small, fast currents from ion channels expressed in *Xenopus* oocytes. *Biophys J* **61**, 78-82 (1992).
11. E. Stefani, F. Bezanilla, Cut-open oocyte voltage-clamp technique. *Methods Enzymol* **293**, 300-318 (1998).
12. A. Pantazis, R. Olcese, "Cut-Open Oocyte Voltage-Clamp Technique" in Encyclopedia of Biophysics, G. Roberts, A. Watts, Eds. (Springer, Berlin, Heidelberg, 2019), 10.1007/978-3-642-35943-9\_371-1, pp. 1-9.
13. C. S. Gandhi, R. Olcese, The voltage-clamp fluorometry technique. *Methods Mol Biol* **491**, 213-231 (2008).